



The *Drosophila* ZNRF1/2 homologue, *detour*, interacts with HOPS complex and regulates autophagy

Shannon Nicolson¹, Jantina A. Manning¹, Yoon Lim¹, Xin Jiang¹, Erica Kolze^{1,2}, Sonia Dayan¹, Ruchi Umargamwala¹, Tianqi Xu¹, Jarrod J. Sandow^{3,4}, Andrew I. Webb^{3,4}, Sharad Kumar ^{1,2}✉ & Donna Denton ¹✉

Autophagy, the process of elimination of cellular components by lysosomal degradation, is essential for animal development and homeostasis. Using the autophagy-dependent *Drosophila* larval midgut degradation model we identified an autophagy regulator, the RING domain ubiquitin ligase CG14435 (*detour*). Depletion of *detour* resulted in increased early-stage autophagic vesicles, premature tissue contraction, and overexpression of *detour* or mammalian homologues, ZNRF1 and ZNRF2, increased autophagic vesicle size. The ablation of ZNRF1 or ZNRF2 in mammalian cells increased basal autophagy. We identified *detour* interacting proteins including HOPS subunits, deep orange (*dor*/VPS18), Vacuolar protein sorting 16A (VPS16A), and light (*lt*/VPS41) and found that *detour* promotes their ubiquitination. The *detour* mutant accumulated autophagy-related proteins in young adults, displayed premature ageing, impaired motor function, and activation of innate immunity. Collectively, our findings suggest a role for *detour* in autophagy, likely through regulation of HOPS complex, with implications for healthy aging.

¹Centre for Cancer Biology, University of South Australia, Adelaide, SA 5001, Australia. ²Faculty of Health and Medical Sciences, The University of Adelaide, Adelaide, SA 5001, Australia. ³The Walter and Eliza Hall Institute of Medical Research, Parkville, VIC 3052, Australia. ⁴Department of Medical Biology, University of Melbourne, Parkville, VIC 3052, Australia. ✉email: sharad.kumar@unisa.edu.au; donna.denton@unisa.edu.au

Macroautophagy (hereafter referred to as autophagy) is a lysosomal degradation pathway that provides cellular quality control by removing cytoplasmic cargos including dysfunctional organelles, protein aggregates and pathogens^{1,2}. The material is engulfed by a double membrane vesicle, the autophagosome, that fuses with the lysosome where the contents are degraded. Disruption of autophagy, including the age-dependent decline in activity, contributes to the pathogenesis of several human diseases^{2–5}. In particular, genetic studies have revealed that defective autophagy causes progressive neurodegenerative phenotypes highlighting the importance of autophagy for the clearance of abnormal protein aggregates^{6–12}. Conversely, enhanced autophagy can result in increased lifespan supporting a role for autophagy in promoting neuronal health^{13,14}. This highlights the critical function of autophagy in neuronal homeostasis and healthy aging. Identifying new regulators of this process has the potential to enable modulation of autophagy to protect against disease.

An integral step in autophagic flux is the fusion of the autophagosome with the lysosome, forming autolysosomes, regulated by the homotypic fusion and vacuole protein sorting (HOPS) tethering complex^{15,16}. The conserved HOPS complex comprises Vacuolar Protein Sorting 11 (VPS11), VPS16, VPS18, VPS33, that are also common subunits of class C core vacuole/endosome tethering CORVET complex, and VPS39 and VPS41, that are unique to HOPS complex^{17,18}. In addition to mediating fusion between autophagosome and lysosome, HOPS complex also regulates fusion of endosomes with lysosomes. The depletion of VPS41 impairs HOPS-dependent delivery of endocytic cargo to lysosomes and causes a defect in autophagic flux^{19,20}. A block in autophagic flux is also observed upon knockdown or mutation of other HOPS subunits in mammalian cells^{14,16,21,22}. In *Drosophila*, cells depleted of each HOPS subunit have impaired autophagic flux²⁰. Recently, mutations in VPS41 were identified in patients displaying neurodegenerative disease, representing a new class of lysosomal disorders²³. Thus, regulation of the rate of fusion between the autophagosome and lysosome is important in maintaining cellular homeostasis and normal physiology. However, many aspects regarding the regulation of autophagy and the interplay with the endolysosomal network in a physiological setting remain poorly understood.

Autophagy plays context-dependent roles during development and has important functions under both basal conditions and in response to stress. The induction of autophagy in response to stress needs to occur rapidly and is tightly controlled by post-translational modifications (PTMs). A key mechanism for regulation of autophagy is ubiquitination of several core components of the autophagy machinery (e.g., ULK1 and PI3K complexes)^{24,25}. Ubiquitin ligases (E3s), together with their interacting proteins, regulate autophagy-related proteins and regulatory components to fine-tune autophagic flux, not only through ubiquitin-mediated proteasomal degradation but also by non-degradative ubiquitin signals. For example, the kinase activity of ULK1, required for autophagy induction, is regulated by the RING-type E3s, tumour necrosis factor receptor (TNFR)-associated factor 6 (TRAF6) and Tripartite motif-containing 32 (TRIM32), which interact with ULK1 via Autophagy and Beclin 1 Regulator 1 (AMBRA1)^{26,27}. AMBRA1 is also a substrate adaptor of CUL4 E3s and both AMBRA1 CUL4 ligase and TRAF6 mediate K63-ubiquitination of Beclin 1 (Atg6), promoting autophagy^{28,29}. Contrary to TRAF6, the deubiquitinating enzyme TNFAIP3/A20 (TNF alpha induced protein 3) reduces K63-linked ubiquitination of Beclin 1, limiting the autophagy response²⁸. As with autophagy initiation, E3s plays an important role in autophagy termination. Following autophagy induction, AMBRA1 phosphorylation by ULK1 results in its

dissociation from the CUL adaptor DNA damage-binding protein 1 (DDB1) and subsequent stabilisation. AMBRA1 is then free to positively regulate autophagy by increasing ULK1 activity and decreasing mTOR activation^{27,30}. Following prolonged starvation, AMBRA1 is ubiquitinated by DDB1/CUL4 and degraded leading to autophagy termination³⁰. Autophagy termination is also regulated by Cullin E3 complexes. The K48-linked ubiquitination of ULK1 by CUL3 with adaptor KLHL20, mediates its proteasomal degradation as well as the degradation of other autophagy machinery components³¹.

Although our understanding of the role of ubiquitination in regulation of autophagy has greatly increased, from phagophore nucleation to autophagosome fusion with the lysosome and termination, there are still outstanding questions to be answered. How is the crosstalk between autophagy and other cellular pathways regulated, in particular between the other vesicle pathways, and what roles do E3s have in modulating this? Thus, it is of great importance to identify the E3s involved in regulatory steps of autophagy.

The degradation of the *Drosophila* larval intestine is dependent on autophagy, yet surprisingly only a subset of the canonical autophagy components are essential for this mode of autophagy^{32,33}. This suggests that distinct autophagy regulatory proteins and mechanisms may be required. Ubiquitination is important for autophagy and cell size reduction that accompanies midgut degradation³⁴. To identify the enzymes of the ubiquitin system required for regulating autophagy we screened a collection of RNAi lines for defects in midgut degradation. Here, we identified *Drosophila detour*, that encodes an uncharacterised Really Interesting New Gene (RING) domain-containing protein homologous to mammalian Zinc and RING Finger 1 and 2 (ZNR1 and ZNR2)^{35,36}. Both ZNR1 and ZNR2 have ubiquitin ligase activity and are highly expressed in the nervous system³⁷. Previous studies suggest that ZNR1 and ZNR2 are involved in growth signalling and protein synthesis^{35,38}. However, currently there is no direct evidence linking ZNR1 or ZNR2 to autophagy.

Here, we show that *detour* mutants had increased early-stage autophagic vesicles as well as an accumulation of autophagy-related proteins in young *Drosophila* adults. Overexpression of *detour* and the mammalian homologues, ZNR1 and ZNR2 in the *Drosophila* midgut led to increased autophagic vesicle size. We further show that *detour* interacts with subunits of the HOPS complex, deep orange (*dor*/VPS18), Vps16A (VPS16), and light (*lt*/VPS41), and promotes ubiquitination of these components. This function appears to be conserved in mammals with ZNR2 interacting with VPS18. The HOPS complex activity has been shown to be important in human disease, hence we examined if *detour* was important for age-related health. The *detour* mutant adults displayed premature aging, impaired motor function, and activation of innate immunity, suggesting that *detour* is required for healthy aging. Our data reveal a function of *detour* in autophagy, likely through an interaction with HOPS complex to regulate autophagic vesicle fusion events, which may play a role in longevity.

Results

***Drosophila detour* regulates autophagy.** During *Drosophila* metamorphosis, the larval intestinal tissue is degraded by an autophagy-dependent pathway^{32,39}. The larval intestine cells in the midgut and gastric caeca begin to increase autophagy levels at the onset of degradation (-4 h relative to puparium formation, h RPF), with high levels of autophagy detected by 2 h RPF³². Genetic inhibition of autophagy severely delays midgut contraction resulting in incomplete midgut degradation, while inhibition

of apoptosis by blocking caspase activity does not affect degradation³². Therefore, identifying factors which affect midgut degradation may uncover novel regulators of autophagy. To do this, we screened a collection of RNAi knockdown lines targeting ubiquitination machinery components. The screen utilised larval midgut-specific expression of GFP (using Mex-GAL4 driver) to identify genes, that perturbed gastric caeca and midgut degradation when knocked down. This identified CG14435, that we have referred to as *detour* (*detr*), encoding a RING domain-containing ubiquitin ligase.

To validate the role of *detour* in autophagy-dependent midgut degradation, the original line identified in the screen (*detour*^{Ri270}) and an additional independent RNAi knockdown line (*detour*^{RiGD}) were examined. The level of knockdown was verified by qRT-PCR (Supplementary Fig. 1a). The effect of reduced *detour* expression on midgut degradation was assessed by examining the gastric caeca morphology at the early onset (-4 h RPF) and during midgut degradation (0 h RPF) (Fig. 1a). As the larvae cease feeding and begin emptying their gut contents, the midgut condenses slightly and the first distinct morphological change that can be observed is shortening of the gastric caeca. This is followed by a dramatic change in gut morphology between 2 and 4 h RPF, where the gut contracts to a fraction of its original length and the gastric caeca disappear. The degradation of the midgut can be closely followed by the contraction of the gastric caeca⁴⁰. Quantitation of gastric caeca size showed that both *detour*^{Ri270} and *detour*^{RiGD} had significantly shortened gastric caeca compared to the control at both stages of degradation (Fig. 1a, -4 h RPF and 0 h RPF top and bottom, respectively).

Previous studies have shown a correlation between autophagy and cell size during contraction of the midgut. Inhibition of autophagy results in a failure to undergo cell size reduction, while induction of autophagy decreases cell size^{33,34,39}. The effect of reduced *detour* expression on autophagy was examined at the onset of midgut degradation (-4 h RPF) using the pmCherry-Atg8a marker, as previously described⁴¹. Consistent with the smaller midgut size, *detour*^{Ri270} and *detour*^{RiGD} knockdown lines showed increased mCherry-Atg8a puncta at -4 h RPF (Fig. 1b). This suggests that reduced levels of *detour* expression led to increased autophagic vesicles and premature midgut degradation.

To investigate the autophagy defect, we generated mosaic clones in the midgut that give rise to cells knocked down for *detour* (marked by GFP) adjacent to control cells. The *detour*^{Ri270} knockdown clone cells displayed increased Atg8a puncta compared to the neighbouring control cells at -4 h RPF (Fig. 1c, d). In addition, the cell size was significantly smaller in *detour* knockdown clones compared to the control (Fig. 1c, e). As the initial genetic screen was based on the larval intestine degradation phenotype, we examined a broader role of *detour* in autophagy. During larval development, the fat body, an energy storage and utilisation tissue, acts as a sensor of nutrient status. In response to acute starvation, autophagy is induced in the fat body to promote cell survival, while under normal growth conditions, there are very low levels of autophagy⁴². To determine if *detour* has a broader role in autophagy, its function was examined in the fat body. Clonal knockdown of *detour* in fat body cells resulted in increased autophagic vesicles under normal growth conditions (Supplementary Fig. 1b), a similar phenotype to the midgut. This suggests that *detour* plays a role in autophagy both in cell death and survival during development.

***detour* mutations alter autophagy and disrupt developmental tissue degradation.** To further examine the role of *detour* in autophagy, we generated a *detour*¹ mutant line by imprecise excision of a *Minos* transposon insertion *detour*^{MiET} and a

revertant line *detour*^{rev} by precise excision of the transposable element (Supplementary Fig. 2a). Loss of genomic sequence in *detour*¹ animals and reversion to wild type open reading frame in *detour*^{rev} was confirmed by sequencing the deletion breakpoints and the genomic region, respectively. All lines were backcrossed to *w*¹¹¹⁸ for 6 generations to eliminate any differences in genetic background. The transcript levels were examined by qRT-PCR in adult flies (Supplementary Fig. 2b). The *detour*¹ is a transcript null allele and the *Minos* transposon insertion line *detour*^{MiET} also had significantly reduced mRNA. The precise excision line *detour*^{rev} had similar mRNA levels to *w*¹¹¹⁸ wild type (Supplementary Fig. 2b). All lines were homozygous viable and fertile with no externally visible phenotype in adults.

Initially, we examined the degradation of the larval midgut to confirm the knockdown phenotypes. Midgut morphology was examined during midgut degradation (0 h RPF) (Fig. 2a). The *detour*¹ and *detour*^{MiET} lines showed significantly reduced gastric caeca size compared to the control (Fig. 2a), consistent with that observed in *detour* knockdown midguts (Fig. 1a). Immunostaining for endogenous Atg8a revealed significantly increased accumulation of Atg8a positive puncta in *detour*¹ and *detour*^{MiET} compared to the controls (Fig. 2b). There was a trend for increased puncta size, however this was not significantly different to the controls (Fig. 2b). We also made use of a deficiency (*Df*) that removes *detour* (and several other genes) to generate transheterozygotes and examined autophagy in -4 h RPF larval midguts. Consistent with the homozygous mutants, immunostaining for endogenous Atg8a revealed a significant increase in Atg8a positive puncta in *detour*¹/*Df* and *detour*^{MiET}/*Df* compared to the controls (Supplementary Fig. 2c). Hence the *detour* mutants and knockdown lines have similar phenotypes, resulting in increased autophagic vesicles and midgut degradation.

To further assess the increase in autophagic vesicle, we examined Atg5 puncta formation, an early-stage autophagic vesicle marker. While Atg8 remains associated with autophagosomes, Atg5 is associated with phagophores but not with autophagosomes⁴³. This showed that there was also an increase in Atg5 positive puncta in the *detour*¹ mutant cells compared to the control (Fig. 2c). In addition, the *Drosophila* p62 autophagic receptor and substrate, refractory to sigma P (*ref(2)P*), accumulated in *detour* mutant cells compared to control (Fig. 2d). Under normal conditions, *ref(2)P* is internalised within the autophagosome and degraded by the autolysosome. This suggests that lysosomal degradation of autophagic cargoes may be impaired. This can result from accumulation of autophagosomes or reduced lysosomal function. The function of the lysosome is dependent on an acidic pH for the degradative activity and can be assessed using LysoTracker, a dye that labels acidic vesicles, as well as the processing of lysosomal enzymes, including Cathepsin L. There was no difference in LysoTracker staining in the *detour* mutant compared to control (Supplementary Fig. 2d). In addition, both pro and mature forms of Cathepsin L were detected in the control and *detour* mutant (Supplementary Fig. 2e). This suggests that lysosome function is not altered in *detour* mutant. To determine the rate of autolysosome formation, we examined the colocalisation of Atg8a with GFP-tagged LAMP1 (human LAMP1 fused to GFP detected by immunostaining for GFP). This enables the detection of autophagosomes as Atg8a positive puncta and autolysosomes as dual-labelled Atg8a and LAMP1 positive vesicles⁴⁴ (Fig. 2e). The *detour* mutant cells had an increased number of Atg8a positive puncta, while the number of colocalised Atg8a and LAMP1 positive autolysosomes did not show a corresponding increase (Fig. 2e).

Importantly, ultrastructural analysis showed that the *detour* mutant midgut cells (at -4 h RPF) had an increase in the formation of autophagic vesicles compared to the control based on transmission electron microscope (TEM) analysis (Fig. 2f).

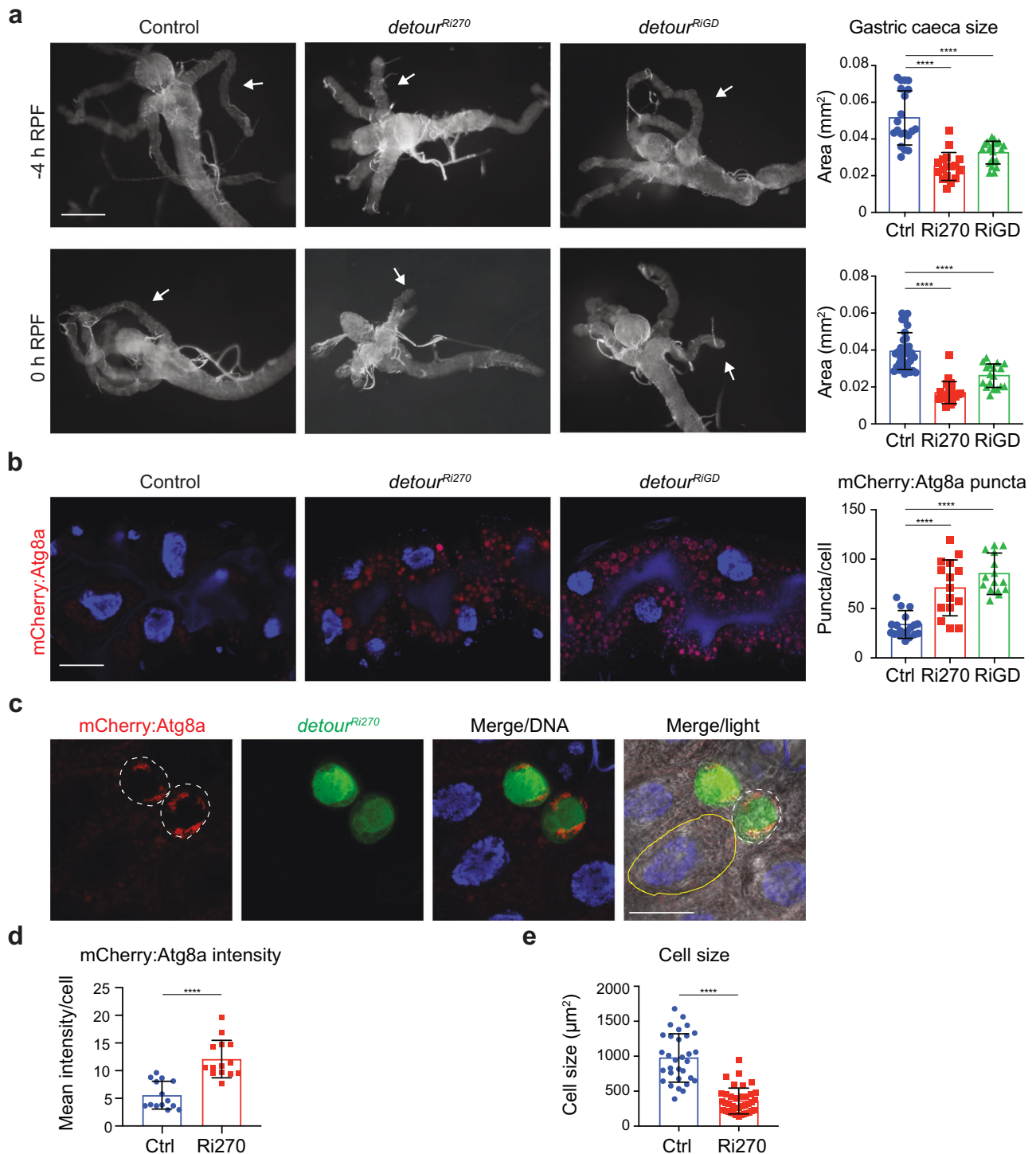
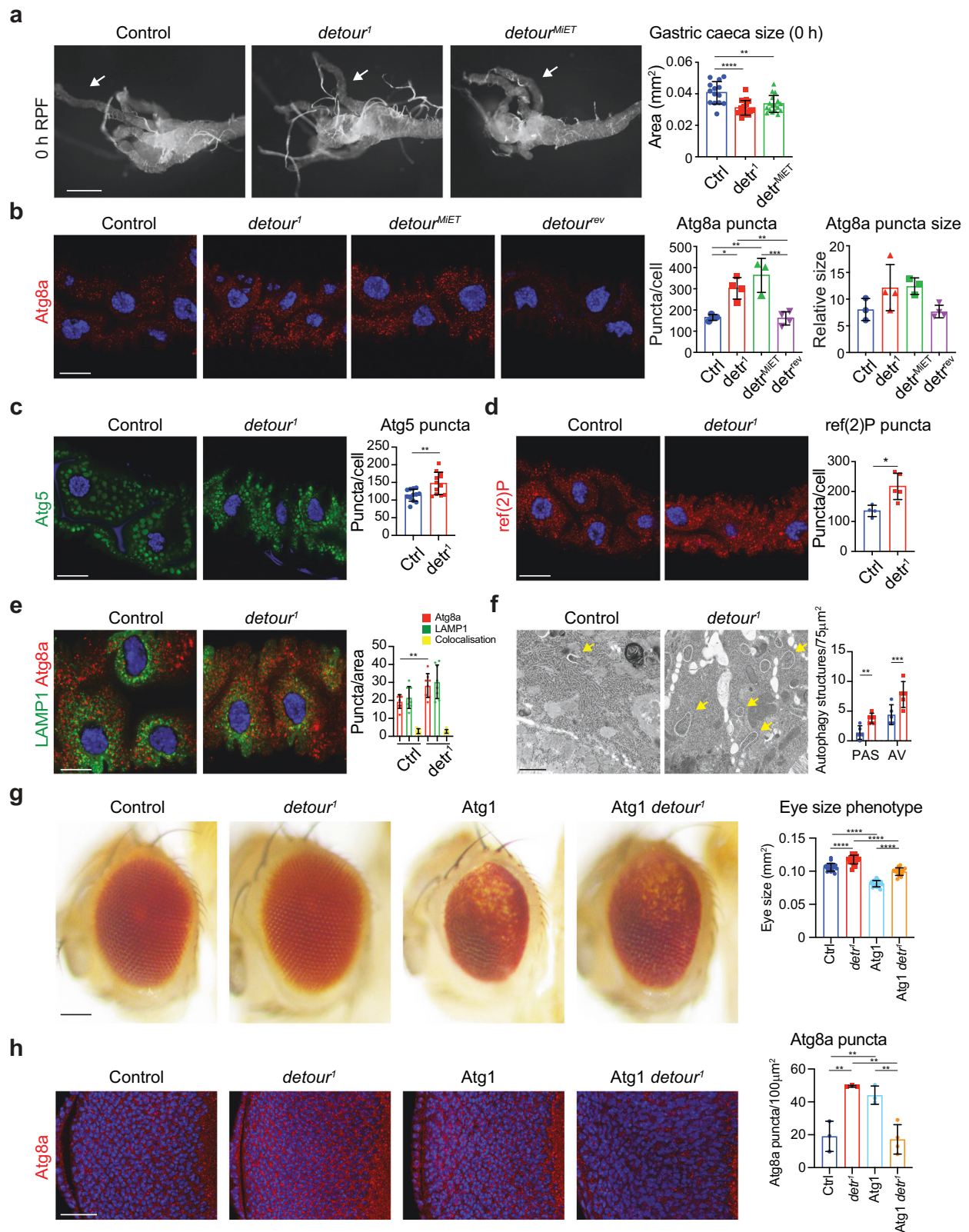


Fig. 1 Knockdown of *detour* increases autophagic vesicles and midgut degradation. **a** Morphology of control (*Mex-GAL4/+; pmCherry-Atg8a/+*), and *detour* knockdown (*Ri270* and *RiGD*) (*Mex-GAL4/+; pmCherry-Atg8a/UAS-detour Ri*) midguts at -4 h and 0 h RPF showed smaller midguts and increased contraction of gastric caeca (arrow). Scale bar = 200 μm. Quantitation of gastric caeca size at -4 h and 0 h RPF. Data presented as area ± SD (*****p* < 0.0001). **b** The knockdown of *detour* has increased mCherry:Atg8a (red) puncta in the larval midguts at -4 h RPF compared to controls (*Mex-GAL4/+; pmCherry-Atg8a/+*). DNA is stained with Hoechst (blue). Scale bar = 20 μm. Quantitation of puncta at -4 h RPF performed using ImageJ. Data presented as average puncta/cell ± SD (*****p* < 0.0001). **c** Clone cells of *detour* knockdown (*hsFLP; pmCherry-Atg8a/+; Act > CD2 > GAL4, UAS-nlsGFP/UAS-detour Ri270*) in the midgut marked by GFP (green) have increased mCherry:Atg8a puncta (red, outlined with dotted line) compared to the neighbouring control cells (non-GFP, outlined with yellow line in merge/light) at -4 h RPF. DNA is stained by Hoechst (blue). Scale bar = 20 μm. **d** Quantitation of mCherry:Atg8a represented as mean intensity/cell ± SD (*****p* < 0.0001). **e** Quantitation of cell size represented as area ± SD (*****p* < 0.0001).



The morphology of these vesicles suggests that they may be at a very early stage of autophagic vesicle formation and accumulate in the *detour* mutant intestine cells without an increase in electron-dense lysosomes. The increase in early-stage autophagosomes (isolation membranes) suggests that closure/maturation may be delayed and/or there is an increase in autophagy

induction. These data suggest an essential role for *detour* in biogenesis of autophagic vesicles in intestine cells.

To further examine the role of *detour* in the autophagy pathway we examined whether *detour* genetically interacts with *Atg1*, which is essential for initiating autophagosome formation (during nutrient stress and development). Overexpression of *Drosophila*

Fig. 2 *detour* mutants have increased autophagic vesicles. **a** Morphology from *detour*¹ and *detour*^{MiET} midguts at 0 h RPF shows reduction in gastric caeca size (arrow) compared to control (*w*¹¹¹⁸). Scale bar = 200 μ m. Quantitation of the gastric caeca size showing significant reduction in *detour*¹ and *detour*^{MiET} compared to control. No significant difference was observed between *detour*¹ and *detour*^{MiET}. Data presented as area \pm SD (*****p* < 0.0001, ***p* = 0.0035). **b** The Atg8a immunostaining (red) of midguts at -4 h RPF shows *detour*¹ and *detour*^{MiET} have similar levels of Atg8a puncta which are both higher compared to the controls (*w*¹¹¹⁸ and *detour*^{rev}). DNA is stained by Hoechst (blue). Scale bar = 20 μ m. Quantitation of Atg8a positive puncta represented as puncta/cell \pm SD (**p* < 0.05, ***p* < 0.01, ****p* < 0.001). Quantitation of Atg8a puncta size represented as average relative puncta size. **c** The eGFP:Atg5 (green) puncta in larval midguts at -4 h RPF is increased in *detour*¹ (*detour*¹/Y; NPI-GAL4/+; UAS-eGFP:Atg5/+) compared to control (*w*¹¹¹⁸/Y; NPI-GAL4/+; UAS-eGFP:Atg5/+). DNA is stained with Hoechst (blue). Scale bar = 20 μ m. Quantitation of puncta represented as average puncta/cell \pm SD (***p* < 0.01). **d** The ref(2)P immunostaining (red) of midguts at -4 h RPF shows *detour*¹ has increased levels compared to the control (*w*¹¹¹⁸). DNA is stained by Hoechst (blue). Scale bar = 20 μ m. Quantitation represented as average puncta/cell \pm SD (**p* < 0.05). **e** The Atg8a (red) and GFP:LAMP (green, anti-GFP) immunostaining of midguts at -4 h RPF shows *detour*¹ (*detour*¹/Y; Mex-GAL4, UAS-GFP:LAMP1/+) has increased Atg8a levels of compared to the control (*w*¹¹¹⁸/Y; Mex-GAL4, UAS-GFP:LAMP1/+). DNA is stained by Hoechst (blue). Scale bar = 10 μ m. Quantitation of Atg8a (red), GFP:LAMP (green) and colocalisation (yellow) represented as average puncta/area \pm SD (***p* < 0.01). **f** Representative TEM images from sections of midgut at -4 h RPF. *detour*¹ midgut cells have increased early autophagic structures (arrows), compared to the control. Scale bar = 1 μ m. Quantitation of autophagic structures, pre-autophagosomal structure (PAS) and autophagic vesicle (AV), represented as average structures/area \pm SD (***p* < 0.01, ****p* < 0.001). **g** Over-expression of the Atg1 in the developing eye (*GMR>Atg1: GMR-GAL4/+; UAS-Atg1/+*) results in a rough eye phenotype, with disruption to patterning, loss of pigmentation and reduced size compared to controls (*GMR w*¹¹¹⁸: *w*¹¹¹⁸/Y; *GMR-GAL4/+* and *GMR detour*¹: *detour*¹/Y; *GMR-GAL4/+*). The Atg1-induced eye phenotype is suppressed by *detour*¹ (*GMR>Atg1 detour*¹: *detour*¹/Y; *GMR-GAL4/+; UAS-Atg1/+*), observed by increased red eye pigmentation and eye size. Scale bar = 100 μ m. The eye size of *GMR detour*¹ is increased compared to the control (*GMR w*¹¹¹⁸). Quantitation of eye size phenotype represented as eye area \pm SD (*****p* < 0.0001). **h** The Atg8a immunostaining (red) of the eye imaginal disc from wandering third instar larvae shows increased Atg8a in both *GMR detour*¹ and *GMR>Atg1* compared to the control (*GMR w*¹¹¹⁸). The combined *GMR>Atg1 detour*¹ results in reduction of Atg8a puncta compared to both *GMR detour*¹ and *GMR>Atg1*. Scale bar = 20 μ m. Quantitation of Atg8a positive puncta represented as puncta/area \pm SD (***p* < 0.01).

Atg1 in the developing eye (using *GMR-Gal4*) induces a high level of autophagy and results in a roughening of the adult eye structure, with disrupted patterning, loss of pigmentation and reduced size compared to the control⁴⁵ (Fig. 2g). We found that the combined *detour*¹ with Atg1 resulted in a less severe eye phenotype compared to Atg1 alone, with an increase in eye pigmentation and reduced disorganisation of the eye pattern resulting in a larger eye size (Fig. 2g). To examine the cellular basis for this, Atg8a positive vesicles were examined in third instar larval eye imaginal disc that gives rise to the adult eye. This revealed that both *detour*¹ and Atg1 had increased Atg8a. Consistent with the reduced severity of the eye phenotype, the combined *detour*¹ Atg1 had Atg8a puncta levels similar to the control (Fig. 2h). This reduction in Atg8a suggest that Atg1 overexpression results in increased Atg8a due to increased induction (increased flux) and *detour* mutant increases Atg8a due to decreased flux with the combination resulting in normal flux. This is also consistent with the role of Atg1 downstream of induction to promote autophagic clearance^{46,47}. Interestingly, the adult eye of *detour*¹ (with *GMR* alone) displayed an increase in size (Fig. 2g), and this was also observed in *detour*¹ hemizygous males compared to *w*¹¹¹⁸ males (Supplementary Fig. 2f). The genetic interactions identified between *Drosophila* Atg1 and *detour* supports the role of *detour* in autophagy. Taken together, this suggests that *detour* may function to regulate autophagy and that the increased phagophores and autophagosomes in *detour* mutants is due to a block in the late-stage autophagy process and the accumulation of autophagic vesicles.

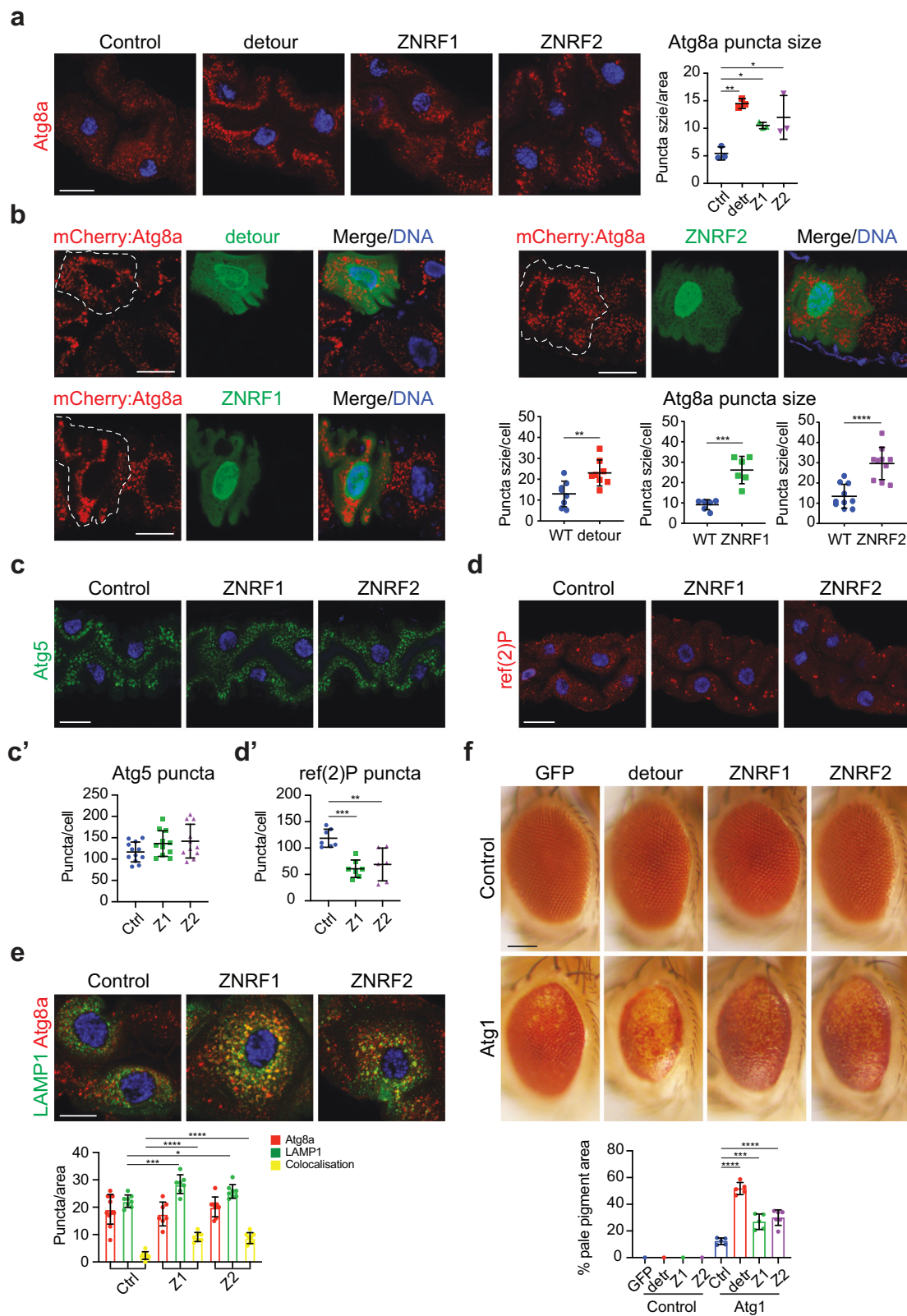
Expression of *detour* and mammalian ZNRF1 and ZNRF2 affects autophagic vesicle size in *Drosophila*. The mammalian homologues of *Drosophila detour* are ZNRF1 and ZNRF2, closely related members of the RING superfamily of ubiquitin ligases. Previous studies suggest that ZNRF1 and ZNRF2 are involved in growth signalling, and ubiquitination^{35,38,48,49}. However, there is no direct evidence for a specific role of ZNRF1 or ZNRF2 in autophagy. To examine the potential conservation of autophagy regulatory function, we overexpressed *detour*, ZNRF1 or ZNRF2 in the *Drosophila* larval midgut. Although this did not affect the contraction of the gastric caeca (Supplementary Fig. 3a), it resulted in an increase in Atg8a positive puncta size, both

immunostaining and live mCherry-Atg8a, at -4 h RPF (Fig. 3a; Supplementary Fig. 3b).

To investigate the increased autophagic vesicle size, we generated clones in the midgut that give rise to cells that overexpressed *detour*, ZNRF1 or ZNRF2 (marked by GFP) adjacent to control cells (Fig. 3b). The *detour* expressing cells were similar in size compared to the neighbouring wild type cells but had increased size of mCherry-Atg8a puncta at -4 h RPF (Fig. 3b). Likewise, clone cells expressing ZNRF1 or ZNRF2 in the midgut were similar in size compared to the neighbouring control cells and also displayed increased size of mCherry-Atg8a puncta at -4 h RPF (Fig. 3b). These results suggest that overexpression of *detour*, ZNRF1 or ZNRF2 causes increased autophagic vesicle size. This was surprising, as the ablation of *detour* results in increased autophagic vesicles, with early stage phagophores and autophagosomes, while the overexpression promotes accumulation of larger autophagic vesicles. This suggests that increasing or decreasing *detour* activity alters autophagic flux.

To further assess the increase in Atg8a positive puncta, the level of GFP:Atg5 positive puncta was examined in ZNRF1 and ZNRF2 expressing midgut cells (not in *detour*:GFP due GFP-tag). There was no increase in Atg5 positive puncta in the ZNRF1 or ZNRF2 overexpression cells compared to the control (Fig. 3c, c'). In addition, ref(2)P levels were reduced in ZNRF1 or ZNRF2 expressing cells compared to control (Fig. 3d, d'), suggesting an increase in degradation by the autolysosome. To determine the rate of autolysosome formation, we examined the colocalisation of Atg8a with GFP:LAMP1. The ZNRF1 and ZNRF2 expressing cells had an increased number of colocalised Atg8a and LAMP1 positive autolysosomes compared to the control (Fig. 3e). In addition, the total number of lysosomes was also increased, supporting an increase in autolysosomes.

Given the genetic interaction between *detour* and Atg1, we further examined the role of *detour*, ZNRF1 and ZNRF2 in autophagy by examining the genetic interaction with Atg1 (Fig. 3). We found that the co-expression of *detour*, ZNRF1 or ZNRF2 with Atg1 resulted in a more severe eye phenotype, compared to Atg1 alone, with a further decrease in eye pigmentation and disorganisation of the eye pattern (Fig. 3f). The expression of *detour*, ZNRF1 or ZNRF2 alone in the eye displayed only a very minor disruption to patterning with no



pigment loss (Fig. 3f). The genetic interactions identified between *Drosophila* Atg1 and ZNRF1, ZNRF2 and detour supports their conserved role in the regulation of autophagy, and suggests that they act to further promote the activity of the autophagy pathway.

ZNRF1 and ZNRF2 maintain basal autophagy. To investigate the role of ZNRF1 and ZNRF2 in autophagy in mammals, CRISPR-Cas9 knockout (KO) HeLa cells were generated. DNA sequencing analysis confirmed biallelic mutations, 1 bp insertion and 56 bp deletion for ZNRF1 KO clone (B8) (Supplementary Fig. 4a–c). The

Fig. 3 Overexpression of detour, ZNRF1 or ZNRF2 increases autophagic vesicle size. **a** Immunostaining of larval midguts at -4 h RPF overexpressing detour (*Mex-GAL4/+; UAS-detour:GFP/+*), ZNRF1 (*Mex-GAL4/UAS-ZNRF1*) or ZNRF2 (*Mex-GAL4/UAS-ZNRF2*) show increased Atg8a (red) puncta size compared to control (*Mex-GAL4/+*). DNA is stained with Hoechst (blue). Scale bar = 20 μ m. Quantification of Atg8a puncta size, measured in ImageJ. Data presented as average puncta \pm SD ($*p < 0.05$, $**p < 0.001$). **b** Clone cells overexpressing detour (*hsFLP; pmCherry-Atg8a/+; Act > CD2 > GAL4, UAS-nlsGFP/UAS-detour:GFP*), ZNRF1 (*hsFLP; pmCherry-Atg8a/UAS-ZNRF1; Act > CD2 > GAL4, UAS-nlsGFP/+*) or ZNRF2 (*hsFLP; pmCherry-Atg8a/UAS-ZNRF2; Act > CD2 > GAL4, UAS-nlsGFP/+*) in the midgut marked by GFP (green) have increased mCherry:Atg8a puncta size (red, clone outlined) compared to the neighbouring control cells at -4 h RPF. DNA is stained by Hoechst (blue). Scale bar = 10 μ m. Quantification of mCherry:Atg8a puncta size in GFP-clone cells and neighbouring wildtype cells. Minimum of $n = 6$ cells. Average puncta size/cell \pm SD ($**p = 0.0059$, $***p = 0.0002$, $****p < 0.0001$). **c** The eGFP:Atg5 (green) puncta in larval midguts at -4 h RPF in ZNRF1 (*NPI-GAL4/UAS-ZNRF1; UAS-eGFP:Atg5/+*) and ZNRF2 (*NPI-GAL4/UAS-ZNRF2; UAS-eGFP:Atg5/+*) is similar to the control (*NPI-GAL4/+; UAS-eGFP:Atg5/+*). DNA is stained with Hoechst (blue). Scale bar = 20 μ m. **d** The ref(2)P immunostaining (red) of ZNRF1 (*Mex-GAL4/UAS-ZNRF1*) and ZNRF2 (*Mex-GAL4/UAS-ZNRF2*) midguts at -4 h RPF shows reduced levels compared to the control (*Mex-GAL4/+*). DNA is stained by Hoechst (blue). Scale bar = 20 μ m. **e** Quantitation of GFP:Atg5 puncta from (c) represented as average puncta/cell \pm SD. **d'** Quantitation of ref(2)P puncta from (d) represented as average puncta/cell \pm SD ($**p < 0.01$, $***p < 0.001$). **e** The Atg8a (red) and GFP:LAMP (green, anti-GFP) immunostaining of midguts at -4 h RPF shows ZNRF1 (*Mex-GAL4, UAS-GFP:LAMP1/UAS-ZNRF1*) and ZNRF2 (*Mex-GAL4, UAS-GFP:LAMP1/UAS-ZNRF2*) have increased colocalisation (yellow) compared to the control (*Mex-GAL4, UAS-GFP:LAMP1/+*). DNA is stained by Hoechst (blue). Scale bar = 10 μ m. Quantitation of Atg8a (red), GFP:LAMP (green) and colocalisation (yellow) represented as average puncta/area \pm SD ($**p < 0.01$). **f** Over-expression of detour (*GMR-GAL4/+; UAS-Atg1/UAS-detour:GFP*), ZNRF1 (*GMR-GAL4/UAS-ZNRF1; UAS-Atg1/+*) or ZNRF2 (*GMR-GAL4/UAS-ZNRF2; UAS-Atg1/+*) in the developing eye results in mild patterning disruption compared to control (*GMR-GAL4/UAS-eGFP*) (top panels). Over-expression of the Atg1 in the developing eye (*GMR-GAL4/+; UAS-Atg1/+*) results in a rough eye phenotype, with disruption to patterning, loss of pigmentation and reduced size compared to control. The Atg1-induced eye phenotype is enhanced by overexpression of detour (*GMR-GAL4/+; UAS-Atg1/UAS-detour:GFP*), ZNRF1 (*GMR-GAL4/UAS-ZNRF1; UAS-Atg1/+*) or ZNRF2 (*GMR-GAL4/UAS-ZNRF2; UAS-Atg1/+*), observed by the loss of red eye pigmentation (bottom panels). Scale bar = 100 μ m. Quantitation of the pale eye pigmentation phenotype represented as percentage \pm SD ($****p < 0.0001$).

introduction of these insertion-deletions caused a frameshift mutation in *ZNRF1* (Supplementary Fig. 4b, c), which resulted in reduced mRNA expression (Supplementary Fig. 4d). Immunoblot analysis and immunostaining confirmed loss of ZNRF2 protein in ZNRF2 KO clone (D9) (Supplementary Fig. 4e, f).

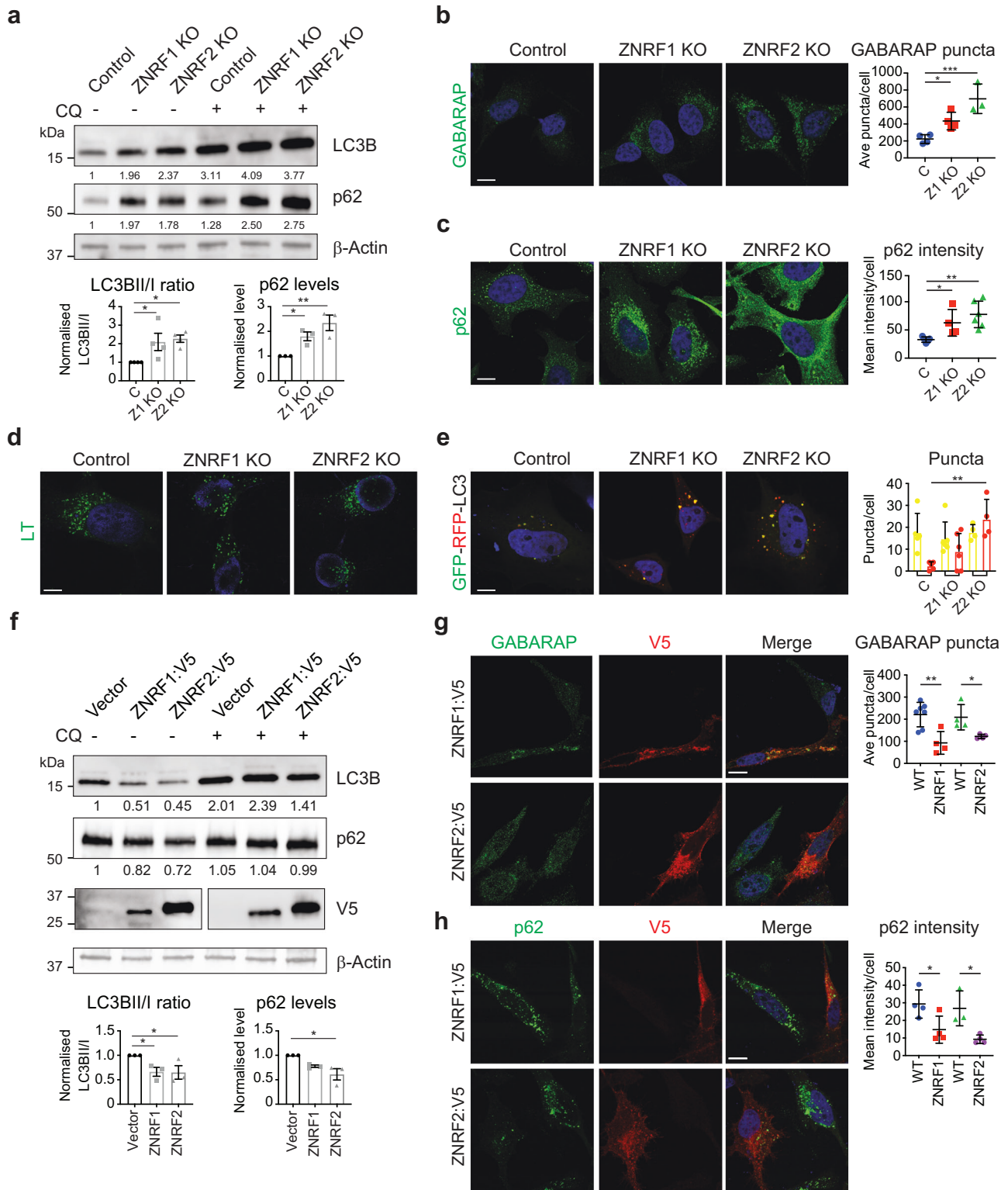
The basal level of autophagy was examined in the *ZNRF1* and *ZNRF2* KO HeLa cell lines. Under normal growth conditions, *ZNRF1* and *ZNRF2* KO cells had increased LC3B lipidation (LC3-II) compared to control cells (Fig. 4a). The autophagy adaptor p62 (*Drosophila* ref(2)P) recruits ubiquitinated cargoes to autophagic membranes. Importantly, ZNRF1 and ZNRF2 KO cells had significantly increased p62 level compared to control cells (Fig. 4a). Moreover, the presence of chloroquine to block lysosomal function further increased LC3B and p62 levels (Fig. 4a).

Consistent with this, there was an increase in autophagic vesicles (GABARAP) in the *ZNRF1* and *ZNRF2* KO cells (Fig. 4b). Similarly, there was increased p62 in both the KO cell lines, with a significantly increased fluorescence intensity in the *ZNRF1* and *ZNRF2* KO cells compared to the control cells (Fig. 4c). In the presence of chloroquine, p62 immunostaining was increased further in the ZNRF1 and ZNRF2 KO cells (Supplementary Fig. 4g). This suggests that there is an increase in basal autophagy in the ZNRF1 and ZNRF2 KO cells. Increased p62 and lipidated LC3B levels can also result from reduced lysosomal function. There was no alteration to LysoTracker staining in the ZNRF1 and ZNRF2 KO cells compared to the control (Fig. 4d). Similarly, there was similar levels of the lysosomal enzyme Cathepsin L activity between control, ZNRF1 KO and ZNRF2 KO cells (Supplementary Fig. 4h) suggesting that lysosome function was not affected. To determine the rate of autolysosome formation, a tandem-tagged GFP-RFP-LC3 reporter was used where dual fluorescence of both GFP and RFP reflects autophagosomes and RFP alone reflects autolysosomes. In ZNRF1 and ZNRF2 KO cells transfected with the reporter, there was an increase in the total number of autophagic vesicles compared to the control (Fig. 4e). There was a significant increase in autolysosomes (RFP alone) in the ZNRF2 KO cells compared to the controls (Fig. 4e). These data show that there is an increase in autophagic flux in *ZNRF1* and *ZNRF2* KO HeLa cells.

We next determined if the expression of ZNRF1 and ZNRF2 was sufficient to reduce the levels of autophagy. The basal level of autophagy was examined in ZNRF1 and ZNRF2 over-expression in HeLa cells. Under normal growth conditions, expression of ZNRF1 and ZNRF2 resulted in reduced LC3B compared to the control cells (Fig. 4f). The level of p62 was significantly reduced in ZNRF2 cells compared to control cells (Fig. 4f). In the presence of chloroquine there was an accumulation of LC3B and p62 (Fig. 4f). The overexpression of ZNRF1 and ZNRF2 reduced the levels of autophagic vesicles (GABARAP) (Fig. 4g). Similarly, there was a decrease in the abundance of p62 in both in the ZNRF1 and ZNRF2 expressing cells (Fig. 4h). These findings are consistent with our observations in *detour* mutant flies and suggest that there is altered autophagic flux in the absence of ZNRF1 and ZNRF2. Similar to that observed in *Drosophila*, ZNRF1 and ZNRF2 may also regulate the rate of autophagosome biogenesis in higher organisms.

Identification of detour interacting proteins. Loss of *detour*, *ZNRF1* or *ZNRF2* resulted in altered autophagic flux (Figs. 1, 2, 4), yet the mechanisms by which *detour* functions in autophagy is not established. To provide insights into its role in autophagy, we identified proteins that interact with *detour* using immunoprecipitation and mass spectrometry (IP-MS) of soluble protein extracts from *Drosophila* S2 cells that expressed *detour:GFP* or GFP alone. Pairwise comparisons between *detour:GFP* and GFP, and between *detour:GFP* and the *detour:GFP* input identified 157 candidate interacting proteins. These proteins were enriched by more than four-fold compared to GFP, had a p -value of ≤ 0.05 and were identified in at least two of the three replicates (Fig. 5a).

Bioinformatic analysis of the data revealed biological processes (BP) associated with *detour* that may be relevant to its role in autophagy (Fig. 5b). The putative *detour*-interacting proteins were subjected to gene ontology (GO)-term enrichment analysis. Of these proteins, 97 were assigned to a BP annotation by DAVID. These proteins were associated with eight BP annotations with intracellular protein transport (GO:0006886) being the most enriched. The other BP annotations included mitotic cytokinesis (GO:0000281), negative regulation of Notch signalling pathway (GO:0045746), actin filament organisation



(GO:0007015), protein phosphorylation (GO:0006468), neurogenesis (GO:0022008), phagocytosis (GO:0006909) and positive regulation of synaptic growth at the neuromuscular junction (GO:0045887).

The cellular component analysis identified that the putative detour-interacting proteins were significantly associated with the cytoplasm, actin filament and membranous organelles including

the endosome (GO:0005768) (Fig. 5b). Consistently, pathway enrichment analysis using the KEGG database identified endocytosis (Fig. 5b). Intriguingly, three HOPS complex subunits, Vacuolar protein sorting 16A (Vps16A), deep orange (dor) and light (lt), were identified (Fig. 5c). These proteins are the *Drosophila* homologues of the HOPS complex components VPS16, VPS18 and VPS41 respectively. While Vps16A and dor

Fig. 4 ZNRF1 and ZNRF2 maintain basal autophagy in HeLa cells. **a** Immunoblot analysis of LC3B and p62 protein levels in whole cell lysates from control, *ZNRF1* KO and *ZNRF2* KO HeLa cells with or without 4 h of chloroquine (CQ) treatment. β -Actin used as a loading control. Numbers represent quantitation of the shown immunoblot normalised to β -Actin and compared to Control. Three immunoblot replicates were quantified, normalised to β -Actin and graphed as relative expression to WT cell line. Average \pm SD ($*p < 0.05$, $**p < 0.01$). **b** Immunostaining of control, *ZNRF1* and *ZNRF2* KO HeLa cells with GABARAP antibody (green) merged with nuclei stained by Hoechst (blue). Scale bar = 10 μ m. Quantification of GABARAP-positive puncta number using ImageJ software \pm SD ($*p < 0.05$, $**p = 0.001$). **c** Immunostaining of control, *ZNRF1* and *ZNRF2* KO HeLa cells with p62 antibody (green) merged with nuclei stained by Hoechst (blue). Scale bar = 10 μ m. Quantification of p62 fluorescence intensity using photoshop histogram function \pm SD ($**p < 0.01$). **d** LysoTracker staining of control, *ZNRF1* and *ZNRF2* KO HeLa cells merged with nuclei stained by Hoechst (blue). Scale bar = 10 μ m. **e** Control, *ZNRF1* and *ZNRF2* KO HeLa cells transfected with GFP-RFP-LC3 merged with nuclei stained by Hoechst (blue). Scale bar = 10 μ m. Quantification of GFP-RFP-LC3 (yellow) and RFP-LC3 (red) fluorescence represented as puncta/cell \pm SD ($**p < 0.01$). **f** Immunoblot analysis of LC3B and p62 protein levels in whole cell lysates transfected with control (vector), *ZNRF1*:V5 and *ZNRF2*:V5 HeLa cells with or without 4 h of chloroquine (CQ) treatment. β -Actin used as a loading control. Numbers represent quantitation of the shown immunoblot normalised to β -Actin and compared to Control. Three immunoblot replicates were quantified, normalised to β -Actin and graphed as relative expression to WT cell line. Average \pm SD ($*p < 0.05$, $**p < 0.01$). **g** Immunostaining of HeLa cells transfected with *ZNRF1*:V5 and *ZNRF2*:V5 with GABARAP antibody (green), V5 (red), and merged with nuclei stained by Hoechst (blue). Scale bar = 10 μ m. Quantification of GABARAP-positive puncta number using ImageJ software \pm SD ($*p < 0.05$, $**p = 0.001$). **h** Immunostaining of HeLa cells transfected with *ZNRF1*:V5 and *ZNRF2*:V5 with p62 antibody (green), V5 (red), and merged with nuclei stained by Hoechst (blue). Scale bar = 10 μ m. Quantification of p62 fluorescence intensity using photoshop histogram function \pm SD ($**p < 0.01$).

are common subunits of the HOPS and CORVET complexes, It is a HOPS-specific component⁵⁰.

detour interacts with HOPS complex subunits dor, Vps16A and It. We further examined the interaction between *detour* and *dor*, *Vps16A* and *It* by co-immunoprecipitation (co-IP) (Fig. 6a; Supplementary Fig. 5a). To verify the interaction between *detour* and *dor*, we performed a co-IP from *Drosophila* S2 cell lysates co-expressing *detour*:GFP and Flag:*dor*. Flag:*dor* was detected when *detour* was pulled down (Fig. 6a; Supplementary Fig. 5a). We also confirmed an interaction between *detour* and *Vps16A* in cells by co-IP using S2 cells co-expressing *detour*:GFP and Myc:*Vps16A* (Fig. 6a; Supplementary Fig. 5a). Similarly, *detour* and *It* interaction was verified by co-IP in S2 cells co-expressing *detour*:GFP and HA:*It* (Fig. 6a; Supplementary Fig. 5a). None of the HOPS subunits co-IPed with GFP alone (Supplementary Fig. 5a). When all subunits were expressed together, IP of *detour* was able to pull down *dor*, *Vps16A* and *It*, indicating an interaction of *detour* with the HOPS complex (Fig. 6a). Finally, we examined ubiquitination of HOPS components using full-length *detour* and *dor*, *Vps16A* and *It*, demonstrating increased ubiquitination of *dor*, *Vps16A* and *It* (Fig. 6b). The C-terminal region of *detour* contains a RING domain, the putative E3 domain (Supplementary Fig. 2a). To determine the role of the RING in the interaction with the HOPS components we generated a *detour* C-terminal deletion (aa 257–303 deleted). Interestingly, the RING domain deletion of *detour* was still able to interact with *dor* and *Vps16A*, albeit at reduced levels (Fig. 6c). While there was decreased *dor* and *Vps16A* in the presence of *detour* RING domain deletion, there also appeared to be reduced ubiquitination of *dor* and *Vps16A* compared to full-length *detour* (Supplementary Fig. 5b). It is also important to consider that *dor* contains a RING domain that in *VPS18* has been shown to function of an E3⁵¹. Our data supports a role for *detour* in the regulation of the HOPS complex ubiquitination, either directly or indirectly by regulation of another ubiquitin ligase.

The HOPS membrane tethering complex is not only required for the fusion between late endosomes and lysosomes, but it also participates in autophagy by mediating the fusion between autophagosomes and lysosomes^{16,17}. Having identified a role for *detour* in autophagy and an interaction between *detour* and HOPS complex, we examined double labelling of Atg8a autophagy marker with Rab7 to mark membrane-bound compartments of the late endosomes and lysosomes. In the *detour* mutant midguts, Rab7 had minimal colocalisation with the

small Atg8a positive puncta in -4 h RPF midguts (Fig. 6d). This was in stark contrast to the overexpression of *detour*, *ZNRF1* or *ZNRF2* in the *Drosophila* larval midgut that resulted in an increased accumulation of large Rab7 positive vesicles that enclosed large Atg8a positive puncta at -4 h RPF (Fig. 6d). This suggests that *detour* activity promotes HOPS complex function in the fusion of autophagic vesicles with lysosomes and/or late endosomes.

Drosophila deep orange and light are essential for autophagy in the larval midgut. In *Drosophila*, clones depleted of HOPS subunits in the larval fat body accumulate autophagosomes, suggesting an impairment of autophagic flux²⁰. To investigate the role of HOPS in regulation of autophagy in the larval midgut, we generated mosaic clones in the midgut that give rise to cells knocked down for *It* and *dor* (marked by GFP) adjacent to control cells. Both the *It* and the *dor* knockdown clone cells had a dramatic reduction in pmCherry-Atg8a positive vesicles compared to the neighbouring control cells at -4 h RPF (Fig. 7a, b). In addition, the size of *It* and *dor* knockdown clone cells was significantly larger compared to the control cells (Fig. 7a, b). The cell size increase observed in the midgut was not seen in fat body cells²⁰. This suggests an additional role for the HOPS complex, in addition to regulation of autophagosome fusion with the lysosome, upstream of autophagy induction.

To further examine the autophagic defect, knockdown of *It* and *dor* was examined in the midgut. Consistent with the larger cell size, midgut morphology of *It* and *dor* knockdown resulted in significantly larger gastric caeca compared to the control (Supplementary Fig. 6a, 0 h RPF). There was also a dramatic reduction in the level of mCherry-Atg8a positive vesicles in *It* and *dor* knockdown midguts (+2 h RPF) (Supplementary Fig. 6b). The Atg8a staining revealed reduced puncta in *It* knockdown with similar levels of Atg8a puncta in *dor* knockdown, however the puncta morphology was altered compared to the control (Fig. 7c; Supplementary Fig. 6c). This suggests that there is a block in autophagosome fusion with the lysosome due to the absence of mCherry-Atg8a vesicles (autolysosomes) and the presence of Atg8a immunostained positive vesicles (autophagosomes). This increase in cell and tissue size and block in autophagy suggests that HOPS is not only required for autophagosome-lysosome fusion but may play a role upstream of autophagy during midgut degradation.

Previous studies have shown that downregulation of growth signalling is essential for autophagy induction^{41,52}. A marker for growth signalling in the midgut is the localization of

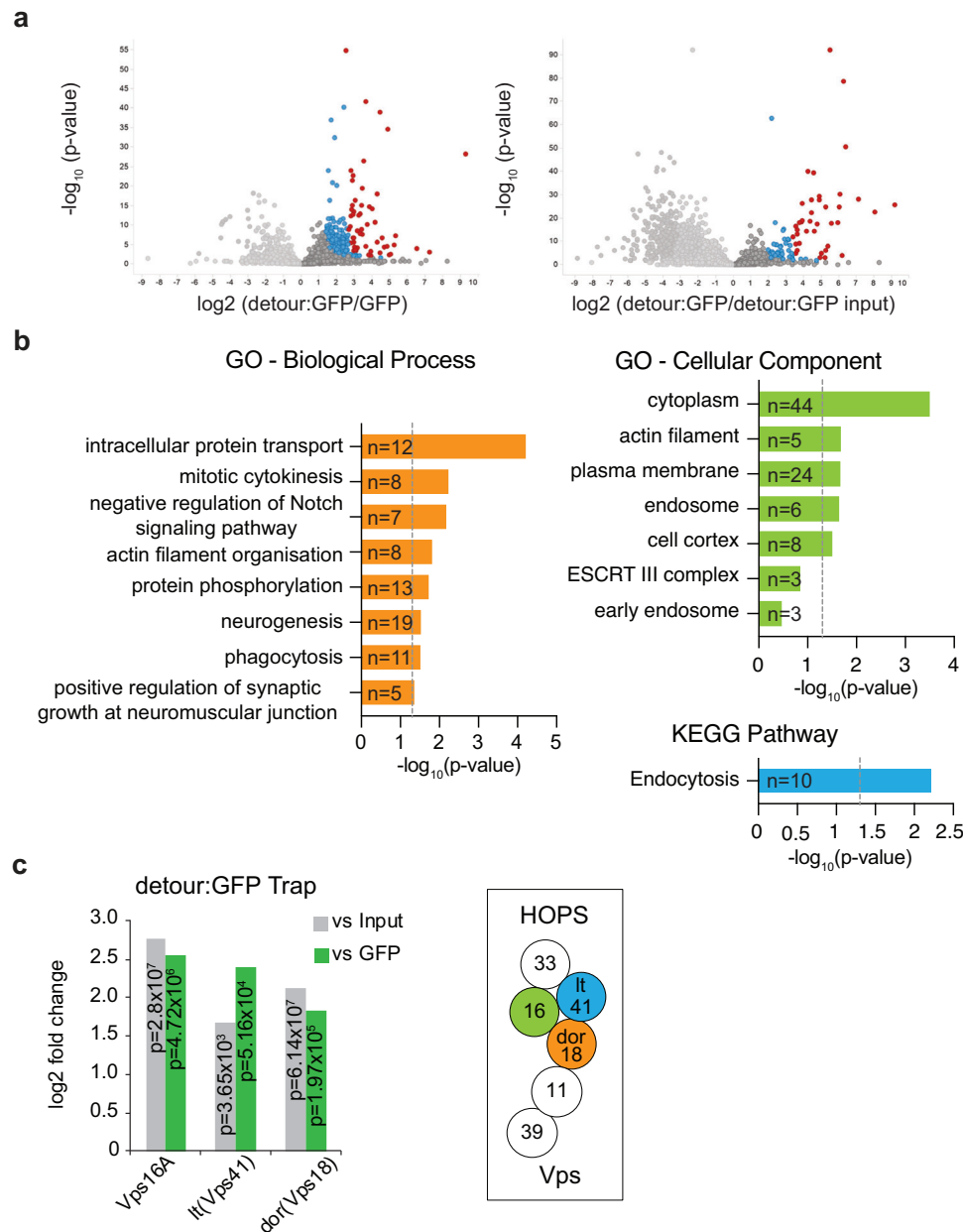
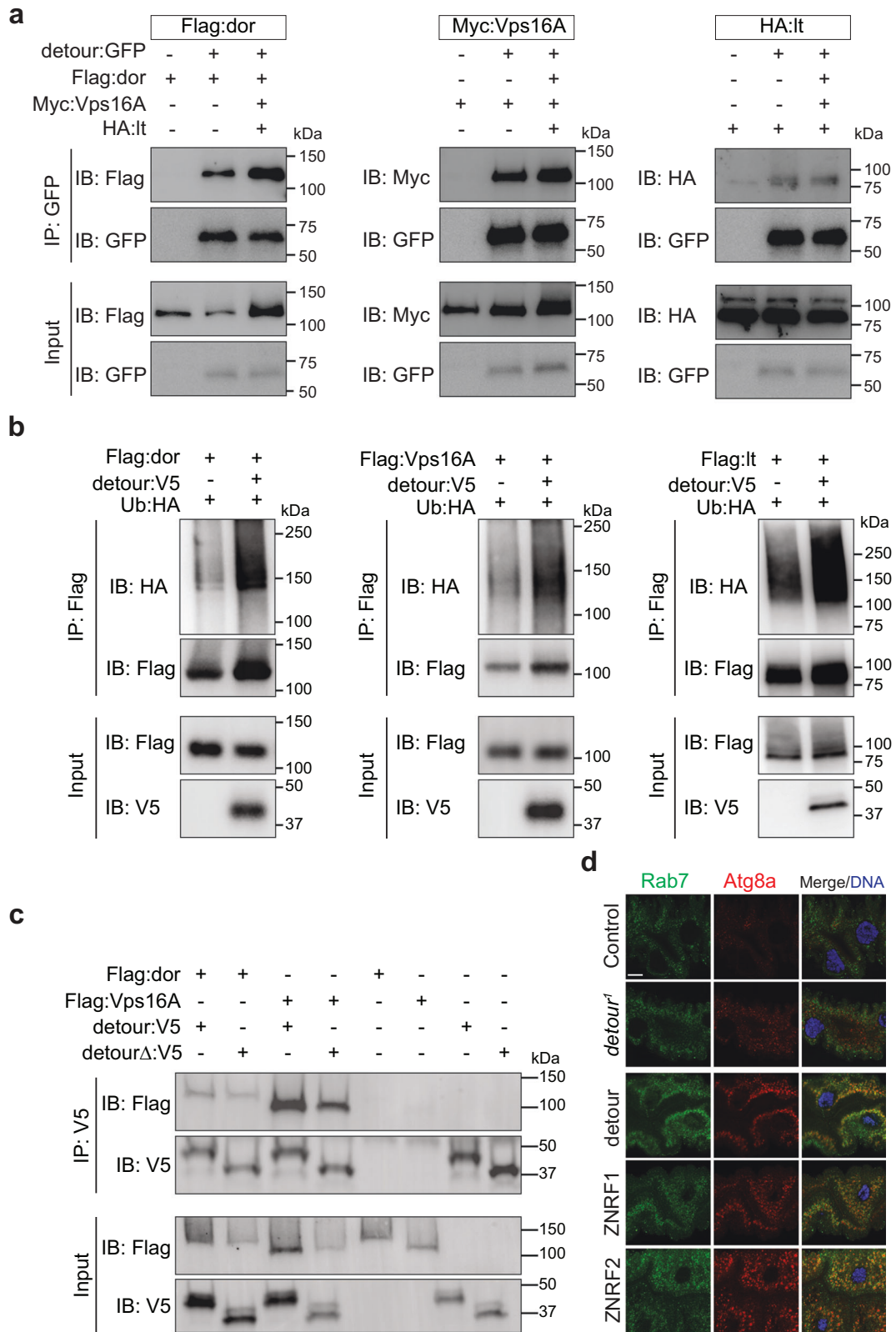


Fig. 5 Identification of detour interacting proteins. **a** Quantitative analysis of detour proteins interacting. Volcano plots showing the estimated log₂ fold changes versus the -log₁₀ p-values for each protein identified as interacting with detour:GFP compared to GFP or detour:GFP input (before immunoprecipitation). Proteins that are highly (4-fold change) and moderately enriched (2-fold change) are shown in red and blue respectively. p-values determined using Mann-Whitney U-test and Benjamini-Hochberg correction. **b** Functional enrichment analysis of candidate detour-interacting proteins. Gene Ontology (GO) analysis of biological processes and cellular components associated with detour:GFP-interacting proteins (n = 157). Pathway enrichment analysis (Kyoto Encyclopaedia of Genes and Genomes, KEGG) of detour:GFP-interacting proteins (n = 157). Vertical dotted line indicates significance cut-off (-log₁₀ of the Benjamini-Hochberg corrected p-value of 0.05), p-values Fisher's exact test. **c** Identification of Vps16A, It/VPS41 and dor/VPS18 from detour:GFP IP-MS. Schematic representation of HOPS complex.

phosphorylated Akt, required for activation of downstream signal transduction. At the onset of midgut degradation (-4h RPF) phosphorylated Akt can be detected at the cell cortex and following puparium formation (+2 h RPF) this cortical localization is greatly reduced⁴¹. Interestingly, the knockdown of *dor* and *It* resulted in persistent cortical localization of phosphorylated Akt in the midgut at +2 h RPF compared to the control with decreased phosphorylated Akt at the cell cortex (Fig. 7d). Together, this data reveals a role for HOPS complex components in the downregulation of growth signalling required for autophagy induction during midgut degradation.

To investigate the in vivo significance of the interaction between detour and HOPS, we examined if there is a genetic interaction between *detour* and *It*, as *It* is a specific component of HOPS. Due to the block in autophagy induction in the *It* knockdown, we examined another independent *It* knockdown line to identify a sensitized genetic background. This line resulted in a decrease in *It* transcript levels in the midgut yet did not result in a detectable midgut phenotype (Supplementary Fig. 6b). In addition, *It* alleles were identified based on an eye pigmentation defect and consistent with the *It^{Ri#2}* line resulting in a weaker knockdown, the eye phenotype of this line (*It^{Ri#2}*) was less severe



compared to that of the strong knockdown line (*lt^{Ri#1}*) (Supplementary Fig. 6c). The effect of simultaneous knockdown of *lt* (*lt^{Ri#2}*) with *detour¹* was examined. Midgut morphology was examined during midgut degradation (0 h RPF) (Fig. 7e). The *detour¹* showed significantly reduced gastric caeca size compared

to the control (Fig. 7e), as expected. Interestingly the combined knockdown of *lt* with *detour¹* increased the gastric caeca size compared to *detour¹* alone (Fig. 7e). To determine if this was due to decreased autophagy, we examined levels of Atg8a positive vesicles. Immunostaining for endogenous Atg8a revealed a

Fig. 6 detour interacts with the *Drosophila* HOPS complex. **a** SL2 cells were co-transfected with GFP-tagged detour and Flag-tagged dor, Myc-tagged Vps16A and HA-tagged It as indicated and subjected to immunoprecipitation (IP) with anti-GFP antibody. Proteins were separated by SDS-PAGE and immunoblotted (IB) with anti-GFP antibody and anti-Flag, anti-Myc or anti-HA antibody. Input controls were 5% of each protein lysate. **b** In the presence of detour there is increased ubiquitination of dor, Vps16A and It in SL2 cells co-transfected with detour, HA-tagged Ub and Flag-tagged dor or Flag-tagged Vps16A or Flag-tagged It as indicated. IPs were carried out using anti-Flag and IB with anti-Flag, anti-HA and anti-V5 antibody. **c** Lysates from SL2 cells co-transfected with V5-tagged detour (detour:V5) or V5-tagged detour RING deletion (detourΔ:V5) and Flag-tagged dor or Flag-tagged Vps16A were subjected to immunoprecipitation (IP) with anti-V5 antibody. Proteins were separated by SDS-PAGE and immunoblotted (IB) with anti-Flag and anti-V5 antibody. Input controls were 5% of each protein lysate. **d** Atg8a and Rab7 staining shows increased Atg8a puncta and enlarged Rab7 positive vesicles in *detour* mutants. Overexpression of detour, ZNRF1 or ZNRF2 have enlarged Atg8a puncta surrounded by Rab7. The Rab7 in detour:GFP was detected with 647 and is coloured green. Scale bar = 20 μm.

significant increase in Atg8a positive staining in *detour*¹, which was reduced when combined with *It* knockdown (Fig. 7f). Given the role of *It* in downregulation of growth signalling, the localisation of phosphorylated Akt was examined. This revealed that *detour* mutant had a dramatic reduction in cortical phosphorylated Akt compared to control at the same stage (Fig. 7g). Interestingly, the combined knockdown of *It* with the *detour* mutant showed an increase in cortically localised phosphorylated Akt (Fig. 7g). Together, these findings indicate that reducing *It* levels is sufficient to restore growth signalling thus reducing autophagy induction and midgut degradation defects in *detour* mutant. This supports an interaction between detour and HOPS complex and suggests that *detour* mutants have decreased HOPS function in the autophagy pathway resulting in delayed autolysosome formation with enhanced HOPS activity to promote downregulation of growth signalling.

detour, ZNRF1 and ZNRF2 interact with HOPS complex. To further examine the interaction between *detour* and HOPS complex, we examined if *detour* genetically interacts with *It*, *dor* and *Vps16A* in the adult eye. HOPS functions in vesicular transport of proteins to pigment granules, the specialised lysosome-related organelle responsible for eye-pigmentation. The knockdown of *It*, *dor* or *Vps16A* in the developing eye (using GMR-Gal4 driver) results in loss of pigmentation compared to the wildtype control (Fig. 8a). We found that knockdown of *It*, *dor* and *Vps16A* combined with *detour*¹ resulted in a less severe eye phenotype, compared to knockdown of *It*, *dor* and *Vps16A* alone, with an increase in eye pigmentation and reduced disorganisation of the eye pattern (Fig. 8a). Furthermore, the combined expression of ZNRF1 and ZNRF2 with the knockdown of *It*, *dor* and *Vps16A* enhanced the eye phenotype with further loss of pigment (Fig. 8a). Interestingly, the reduction of autophagy by *Atg1* knockdown (or *Atg8a* mutant, DNS) was also sufficient to suppress the *It*, *dor* and *Vps16A* knockdown eye phenotypes.

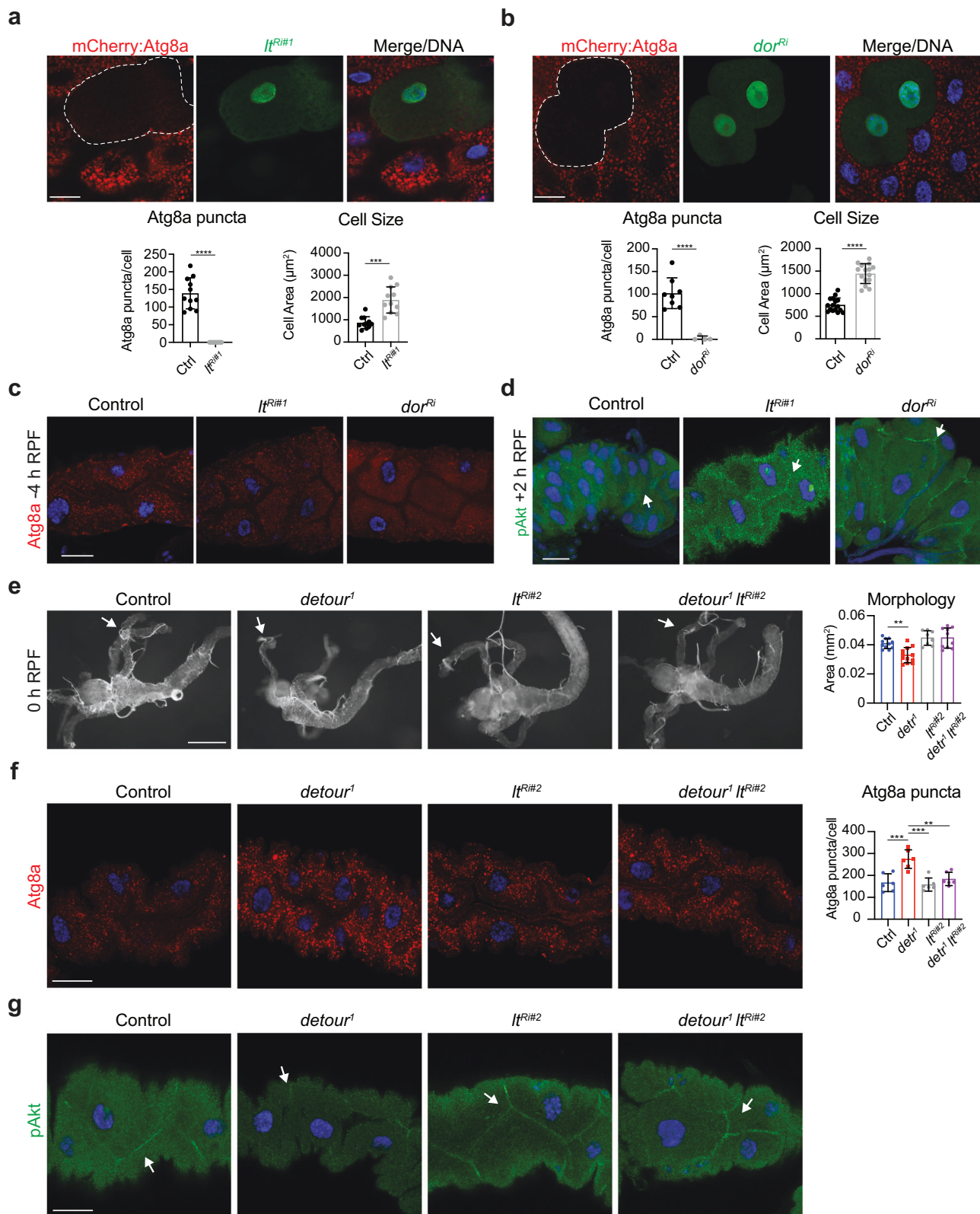
To assess the conserved interaction between ZNRF1 and ZNRF2 with VPS18 in mammalian cells, we examined their colocalisation in HeLa cells transfected with V5-tagged ZNRF1 and ZNRF2. This showed that cytoplasmic ZNRF2 colocalised with VPS18, to a greater extent than ZNRF1 and VPS18 (Fig. 8b). Furthermore, we were able to detect an interaction between ZNRF2 and VPS18 by co-immunoprecipitation of endogenous proteins from HeLa cells (Fig. 8c.) Importantly, the ubiquitination of endogenous VPS18 was reduced in the ZNRF2 KO cells compared to the control (Fig. 8d). The localisation of VPS18 appeared more widespread throughout the cytoplasm in the ZNRF1 KO and this altered distribution was more pronounced in the ZNRF2 KO cells (Fig. 8e). This interaction was specific for ZNRF2 as ZNRF1 did not colocalise with VPS18 and the ZNRF1 KO cells did not significantly alter VPS18 ubiquitination. There was a trend for increased ubiquitination of VPS18 in the ZNRF1 KO cells and this may be due to increased activity of ZNRF2 in the absence of ZNRF1, however this is yet to be confirmed.

Together, these data suggest that the interaction between ZNRF2 and HOPS complex is conserved in mammalian cells. This also indicated that the roles of ZNRF1 and ZNRF2 in autophagy may not be redundant and may have distinct targets in the regulation of autophagy.

detour is required for healthy ageing. Both *detour* mutant alleles are homozygous viable and fertile, with no overt phenotype in the adults. Given the tissue-specific autophagy defects that we observed in the knockdown and mutant during development, we investigated autophagy in *detour* mutant adults. The age-related decline in autophagy in *Drosophila* adults can be monitored by the accumulation of the p62 homologue ref(2)P and Atg8a in old compared to young adults⁵³. Immunoblot analysis showed that the *detour* mutant young adults (day 1) have significantly higher levels of ref(2)P protein than the control flies, and a trend towards increased Atg8a, indicating that autophagy is disrupted (Fig. 9a, b). The accumulation of ref(2)P and Atg8a protein during aging (day 21) was similar between the controls and mutants (Fig. 9a, b; Supplementary Fig. 7a). The mRNA transcript levels of *ref(2)P* and *Atg8a* remained similar between control and mutants in both young and aged adults (Supplementary Fig. 7b), suggesting post-transcriptional regulation. Ref(2)P is a major component of protein aggregates in flies that are defective in autophagy, and in *Drosophila* models of human neurodegenerative diseases⁵⁴. Consistent with this, adult *detour* mutant brain sections had an increase in ref(2)P-positive structures and Atg8a puncta compared with the control brains (Fig. 9c). Interestingly, there is also an accumulation of ref(2)P in the neuropil of the *detour* mutant brains. This is similar to that seen in wild-type aged brains that accumulate ref(2)P in both neuropil and cortical regions⁵⁴. The accumulation of ref(2)P and Atg8a in the young *detour* mutant adults indicates that autophagic flux is disrupted.

Immune activation is triggered by pathogens, and in the nervous system, it can also be triggered by autophagy⁵⁵. In *Drosophila*, impaired autophagic flux induces an immune response, including antimicrobial peptide (AMP) expression^{56–58}, which is a hallmark of many neurodegenerative diseases in humans and may contribute to decline in neuronal function⁵⁵. Given this link, we examined whether impairment of autophagy due to *detour* ablation altered innate immunity. The levels of AMP transcripts *Diptericin A* (*DptA*), *Drosocin* (*Dro*) and *Attacin-A* (*AttA*), under regulation of immune deficiency (IMD) pathway, were examined in the *detour* mutants and control adults. This showed a significant upregulation of AMPs in *detour* adults at both young and older ages compared to the controls (Day 1 and Day 21; Fig. 9d). The expression of AMP genes is increased in *detour* mutant flies as early as 1 day after eclosion, increasing as the flies aged 21 days. There was no difference in the expression of AMP genes following septic injury in *detour* compared to control (Supplementary Fig. 7c).

The overall health and neuronal function of *Drosophila* can be tracked by longevity assays, which reflect the deterioration in



essential cellular processes such as autophagy. Longevity assays showed that *detour*¹ mutant males have a reduced median lifespan compared to controls (Supplementary Fig. 7d). This was confirmed when *detour* mutant animals were crossed to the deficiency (*Df*), with a reduced median lifespan of 33 days for *detour*¹/*Df* and 36 days for *detour*^{MiET}/*Df* compared to controls

with 38 days *w*¹¹¹⁸/*Df* and 43 days *detour*^{rev}/*Df* (Fig. 9e). The median survival of *detour* mutants was shortened as well as the maximum survival. Hence, disruption of *detour* causes dysfunctional autophagy and reduced longevity.

The age-dependent decline in neuronal function can be examined in the adult by measuring the climbing ability as it

Fig. 7 *detour* genetically interacts with *light*. **a** Clone cells knockdown for *lt* (*hsFLP; pmCherry-Atg8a/UAS-ltRi#1; Act > CD2 > GAL4, UAS-nlsGFP/+*) in the midgut marked by GFP (green) has decreased mCherry:Atg8a puncta size (red, clone outlined) and increased cell size compared to the neighbouring control cells at -4 h RPF. DNA is stained by Hoechst (blue). Scale bar = 10 μ m. Quantification of mCherry:Atg8a puncta size represented as average puncta size/cell \pm SD. Quantification of cell size represented as area \pm SD (**** p < 0.0001). **b** Clone cells knockdown for *dor* (*hsFLP; pmCherry-Atg8a/+; Act > CD2 > GAL4, UAS-nlsGFP/UAS-dorRi*) in the midgut marked by GFP (green) has decreased mCherry:Atg8a puncta size (red, clone outlined) and increased cell size compared to the neighbouring control cells at -4 h RPF. DNA is stained by Hoechst (blue). Scale bar = 10 μ m. Quantification of mCherry:Atg8a puncta size represented as average puncta size/cell \pm SD. Quantification of cell size represented as area \pm SD. (**** p < 0.001, **** p < 0.0001). **c** The Atg8a immunostaining (red) of midguts at -4 h RPF from knockdown of *lt* (*Mex-GAL4/UAS-ltRi#1*, strong knockdown line) and *dor* (*Mex-GAL4/+; UAS-dorRi/+*) compared to controls (*Mex-GAL4/+*). DNA is stained with Hoechst (blue). Scale bar = 20 μ m. **d** The phosphorylated Akt (pAkt) immunostaining (green) of midguts at +2 h RPF shows cortical localisation (arrow) in *lt* (*Mex-GAL4/UAS-ltRi#1; pmCherry-Atg8a/+*) and *dor* knockdown (*Mex-GAL4/+; pmCherry-Atg8a/UAS-dorRi*) which is reduced in the control (*Mex-GAL4/+; pmCherry-Atg8a/+*). DNA is stained by Hoechst (blue). Scale bar = 20 μ m. **e** Morphology of control (*w¹¹¹⁸*), *detour¹*, the weak *lt^{Ri#2}* knockdown (*Mex-GAL4/+; UAS-ltRi#2/+*, weak knockdown line) and combined *detour¹ lt^{Ri#2}* knockdown midguts at 0 h RPF. The smaller gastric caeca (arrow) in *detour¹* are rescued by knockdown of *lt*. Scale bar = 200 μ m. Quantification of gastric caeca size at 0 h RPF represented as area \pm SD (** p < 0.01). **f** The Atg8a immunostaining (red) of midguts at -4 h RPF shows increased Atg8a puncta in *detour¹* and *detour¹ lt^{Ri#2}* with similar levels of Atg8a puncta compared to the control (*w¹¹¹⁸*). DNA is stained by Hoechst (blue). Scale bar = 20 μ m. Quantification of Atg8a positive puncta represented as puncta/cell \pm SD (* p < 0.05, ** p < 0.01, **** p < 0.001). **g** The pAkt immunostaining (green) of midguts at -4 h RPF shows reduced cortical localisation (arrow) in *detour¹* compared to the combined *detour¹* with *lt^{Ri#2}* knockdown. DNA is stained by Hoechst (blue). Scale bar = 20 μ m.

reflects the interplay between neuronal and muscular functions. *detour* mutant adults exhibited a climbing defect (<25 mm), that continues to worsen with age, with *detour* consistently displaying a more severe defect than the normal age-related defects in controls, reaching significance at day 21 (Fig. 9f). Consistent with this, the climbing ability (>160 mm), that also declines with age, was significantly reduced in aged (Day 21) *detour* mutants compared to control (Supplementary Fig. 7e). These significant defects in motor function in the *detour* mutant adults suggests that *detour* protects neuronal cells from neurodegeneration.

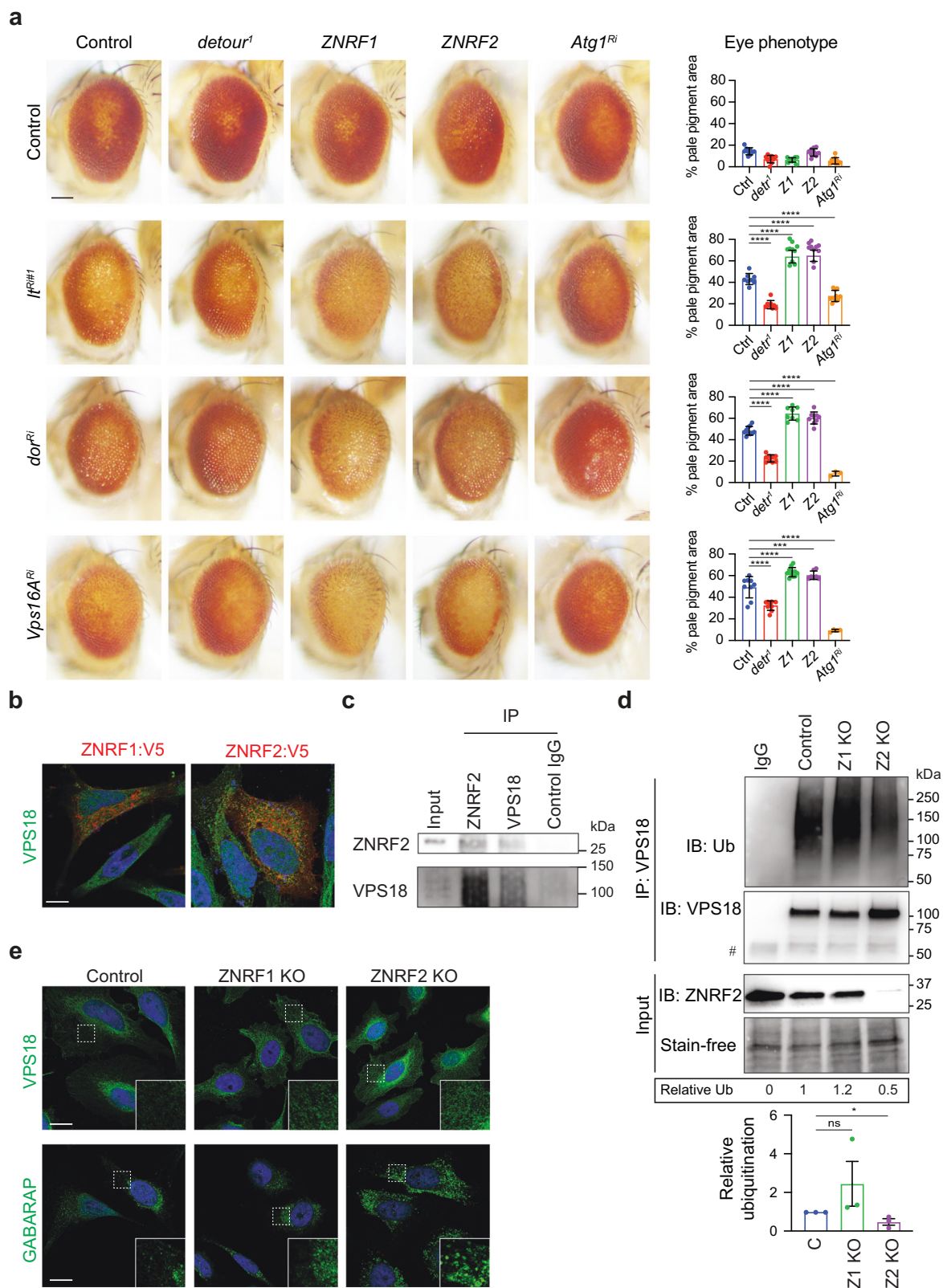
Discussion

To identify new regulators of autophagy, we screened a collection of RNAi lines that knocked down genes encoding proteins of the ubiquitin system for defects in the degradation of the *Drosophila* larval intestine. From this we identified *Drosophila detour*, the orthologue of mammalian ZNRF1 and ZNRF2. The knockdown of *detour* resulted in premature midgut degradation and increased autophagic vesicles. Consistent with this, increased Atg8a levels and smaller cell size was observed in mosaic clone cells ablated for *detour* in the midgut. We generated *detour* mutant lines that also displayed smaller midgut size with increased Atg8a-positive autophagic vesicles. There was also an increase in Atg5-positive vesicles suggesting an increase in early-stage phagophores and an increased ref(2)P suggesting a decrease in cargo transport to the lysosome. Consistent with this, while there was an increase in phagophores and autophagosomes, there was no corresponding increase in autolysosomes. Ultrastructural analysis also revealed an increase in both phagophores and autophagosomes. Furthermore, in the midguts ablated for *detour*, the Atg8a positive puncta appeared to be distinct from Rab7 positive vesicles. This suggests that there is an accumulation of phagophores and autophagosomes and a delay in the formation of autolysosomes in *detour* mutants. In the absence of components of two ubiquitin-like conjugation systems, the E3-like Atg5 or E2-like Atg3, isolation membranes form and persist as open-ended vesicles^{59–61}. However, these vesicles eventually form closed autophagosomes that fuse with lysosomes, indicating that the rate of transition from phagophore to autophagosome is delayed in ATG-conjugation deficient cells⁶². However, as *detour* mutants accumulate both phagophores and autophagosomes without an increase in autolysosomes, this suggests that fusion with the lysosome is delayed. The role of *detour* in autophagy is further supported by the genetic interactions identified between *Drosophila* Atg1 and

detour. Taken together, this supports a role for *detour* as a positive autophagy regulator and that *detour* mutants accumulate autophagic vesicles due to a delay in autolysosome formation.

The overexpression of *detour*, ZNRF1 or ZNRF2 in *Drosophila* midguts led to an increase in autophagic vesicle size, with a decrease in ref(2)P. This is consistent with an increase in autolysosome and the increase in Rab7 and Atg8a positive puncta. This suggests that autophagic vesicle maturation is enhanced following overexpression of *detour*, ZNRF1 or ZNRF2, leading to the accumulation of late stage autophagosomes and/or autolysosomes. The role of *detour*, ZNRF1 and ZNRF2 in modulation of autophagy is supported by the genetic interactions between *detour*, ZNRF1 or ZNRF2 and Atg1. To further establish if the function of *detour* is conserved in mammals, we generated ZNRF1 and ZNRF2 deficient HeLa cells. The ZNRF1 and ZNRF2 KO cells had increased LC3 lipidation with ZNRF2 KO cell also having increased p62. Conversely, their overexpression in HeLa cells was sufficient to reduce p62 levels. This suggests that ZNRF1 and ZNRF2 are required to maintain basal autophagy under normal growth conditions, similar to *Drosophila detour*. These findings suggest that ubiquitin ligases *detour*, ZNRF1 or ZNRF2 promote the fusion of autophagosomes with lysosomes, leading to increased autophagic vesicles due to the accumulation of enlarged autophagosomes and/or autolysosome.

We identified HOPS complex subunits, *dor/VPS18*, *Vps16A* and *lt/VPS41* as interactors of *detour*. Our studies have focused on HOPS due to the interaction with the HOPS specific subunit, *lt*. It is also important to note that as *dor* and *Vps16A* are shared with CORVET the activity of this complex could be examined in future studies. The HOPS complex coordinates the fusion between autophagosomes and lysosomes. The autophagy defects observed following modulation of *detour* are consistent with that due to the altered HOPS complex activity, that similarly results in impaired autophagic flux. We propose that *detour* is required for autophagosome maturation and/or autophagosome-lysosome fusion due to its role in regulating HOPS complex. Furthermore, our study identified an additional role for HOPS complex in downregulation of growth signalling in the *Drosophila* larval midgut. Our results suggest that in the absence of *detour* there is a decrease in autophagosome fusion with the lysosome as well as an increase in autophagy induction. This may be due to premature downregulation of growth signalling as HOPS is now recruited to growth signalling pathway and despite the increased autophagy induction flux is delayed as there is no increase in autolysosomes. This suggests that in the absence of *detour*, HOPS is no longer



tethered to autophagy pathway but is recruited to growth signalling pathway resulting in enhanced downregulation of phosphorylated Akt. The ablation of *detour*, *ZNRF1* or *ZNRF2* may prevent the maturation of autophagic vesicles due to defects in HOPS-dependent membrane fusion events that delay autophagic cargo delivery to lysosomes. The overexpression of *detour*, *ZNRF1* or *ZNRF2* may enhance vesicle fusion between

autophagic vesicles and lysosomes, leading to an accumulation of autolysosomes. We propose that membrane-associated ubiquitin ligases *detour*, *ZNRF1* and *ZNRF2*, through an interaction with HOPS complex, regulate the rate of the delivery of autophagic cargo to the lysosome.

ZNRF1 and *ZNRF2* are closely related members of the RING superfamily of ubiquitin ligases with *detour* the single orthologue

Fig. 8 detour, ZNRF1 and ZNRF2 genetically interact with HOPS subunits. **a** The knockdown of *It^{Ri#1}* (*GMR-GAL4, UAS-It^{Ri#1}/+*), *dor^{Ri}* (*GMR-GAL4+, UAS-dor^{Ri}/+*) and *Vps16A^{Ri}* (*GMR-GAL4, UAS-Vsp16A^{Ri}/+*) in the developing eye results in a pale eye colour phenotype, with loss of pigmentation and reduced size compared to controls (*GMR-GAL4/+*). The pale eye phenotype is suppressed by *detour¹* and *Atg1* knockdown observed by increased red eye pigmentation and eye size. The expression of ZNRF1 and ZNRF2 enhances the *It^{Ri#1}*, *dor^{Ri}* and *Vps16A^{Ri}* eye phenotype. Note that *GMR-GAL4* alone results in a rough eye phenotype at 29°C. Scale bar = 100 µm. Quantitation of eye phenotype represented as eye area ± SD. **b** Immunostaining of HeLa cells transfected with ZNRF1:V5 and ZNRF2:V5 with VPS18 antibody (green), V5 (red), merged with nuclei stained by Hoechst (blue). Scale bar = 10 µm. **c** Total protein lysates from HeLa cells were subjected to immunoprecipitation (IP) with anti-ZNRF2, anti-VPS18 or Control IgG antibody. Proteins were separated by SDS-PAGE and immunoblotted with anti-ZNRF2 antibody or anti-VPS18 antibody. Input controls were 5% of each protein lysate. **d** Decreased ubiquitination of VPS18 in ZNRF2 KO HeLa cells. Total protein lysate from Control, ZNRF1 KO and ZNRF2 KO were subjected to IP with anti-VSP18 or IgG control antibody and immunoblotted with anti-ubiquitin, anti-VPS18 and anti-ZNRF2 antibodies. Numbers represent the quantitation of Ub relative to VPS18 normalised to Control for the representative IB shown. # IgG heavy chain. Quantitation of VPS18 ubiquitination relative to control ±SEM (**p* < 0.05). **e** Immunostaining of control, ZNRF1 and ZNRF2 KO HeLa cells with VPS18 antibody (top panel) and GABARAP (bottom panel) (green) merged with nuclei stained by Hoechst (blue). Scale bar = 10 µm. Dashed outline region is represented in the enlarged inset.

in *Drosophila*. Their E3 RING domains can recruit and tether E2 ubiquitin-conjugating enzyme complexes to regulate the formation of Lys63-ubiquitin or Lys48-ubiquitin linkages^{35,37,38,48,49,63,64}. This Lys63-linked polyubiquitination of proteins can promote membrane trafficking and lysosomal degradation. Both ZNRF1 and ZNRF2 are localised to vesicle membranes by N-myristoylation and this is important for ZNRF2 localisation and interaction with mTORC1^{35,48}. The *S. cerevisiae* homologue, the transmembrane RING domain E3 Pib1, also associates with the target membrane (via interactions with phosphoinositides) and localises to endosomes and vacuoles with a role in vacuolar sorting and multivesicular body pathway^{65,66}. As *detour* also contains a conserved motif for N-myristoylation, this suggests an important evolutionarily conserved membrane-bound E3 family that regulates vesicle fusion events important to maintain autophagic flux.

ZNRF1 and ZNRF2 are present at the neuromuscular junction and strongly expressed in mouse neurons^{36,37}, and ZNRF1 promotes axonal degeneration³⁸. ZNRF2 has been shown to have a protective role in cerebral ischaemia/reperfusion injury in rats⁶⁷. Our findings show that loss of *detour* results in dysfunctional autophagy, with increased expression of AMP genes, motor function defects and decreased lifespan. This indicates that *detour* functions more broadly in maintaining autophagic flux and is important for preventing premature neurodegeneration and promoting healthy aging. Effective autophagic-lysosomal clearance of dysfunctional proteins is particularly important in neuronal cells to maintain homeostasis to prevent neurodegenerative effects throughout their lifespan. The identification of VPS41 mutations in patients with a severe neurological disorder, highlights the important function of HOPS-dependent delivery of autophagic cargo to lysosomes²³. This suggests that ZNRF2 may act to regulate HOPS dependent transport/fusion which will be important for future studies. As there was previously no direct evidence linking ZNRF1 or ZNRF2 to autophagy, this new information raises important questions as to their functions in neurons, particularly under pathogenic conditions.

Based on our findings we propose a model whereby *detour* promotes the recruitment of HOPS to the autophagy pathway and perturbations to *detour* level result in an altered balance of HOPS complex tethering to other organelle localisations. This is supported by both cell biology and genetic interactions. Induction of autophagy can occur, yet the downstream maturation and lysosomal fusion are altered in response to changes in *detour*, ZNRF1 and ZNRF2 levels. In the midgut, *detour* promotes the localisation of HOPS to the autophagy pathway to regulate autophagosome fusion with the lysosome. When *detour* levels are reduced this alters the pool of HOPS acting in the autophagy pathway and facilitates HOPS to act in growth signalling pathway. In the eye, tethering HOPS to the autophagy pathway by

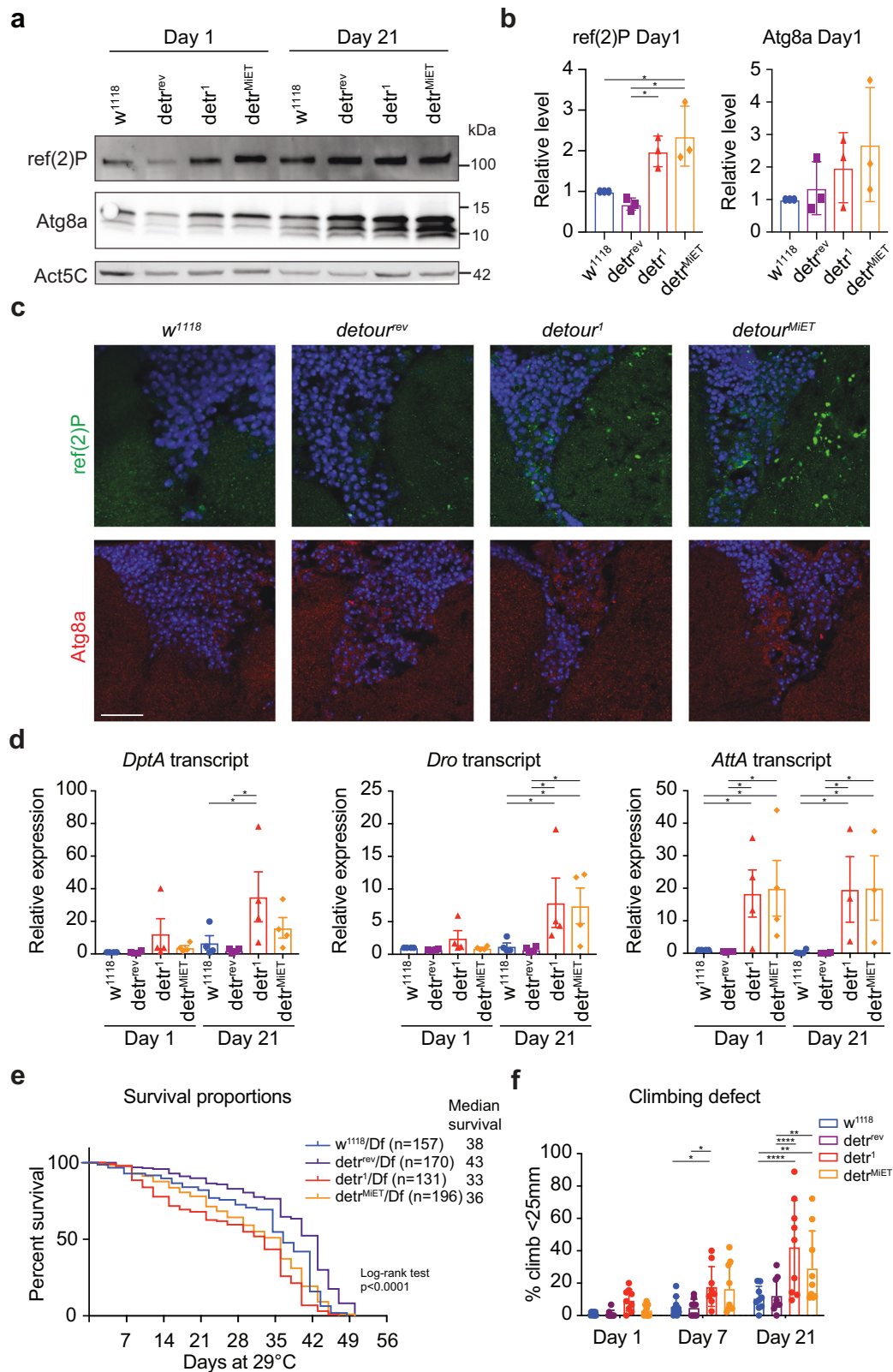
ZNRF1 and ZNRF2 overexpression leads to a reduced pool of HOPS components to act in the eye-pigmentation pathway, resulting in the enhanced eye phenotype. Conversely, in the absence of *detour* HOPS is no longer recruited to autophagy and increases the pool that can act in eye pigmentation. Similarly, reducing autophagy by *Atg1* knockdown, is sufficient to suppress the eye pigmentation defect. This suggests that reduced autophagy and hence reduced role of HOPS complex, results in an increased pool of HOPS to act in the eye pigmentation pathway. Alternative models are also possible, including that autophagy regulation by *detour* may be due to the alteration to growth signalling as seen in the maintained pAKT in the *detour* mutants and given the role of ZNRF2 on mTOR³⁵.

Adaptors play important roles in the recruitment of protein complex to specific cytoplasmic compartments. The Valosin Containing Protein (VCP) is an AAA+ ATPase that localises to several cellular compartments including lysosomes, with mutations linked to several degenerative diseases⁶⁸. The VCP-binding co-factor (SVIP) recruits VCP to lysosomes and is essential for autophagosomal-lysosomal fusion⁶⁹. Mutation in SVIP result in degenerative defects, including declining locomotor activity and decreased life span⁶⁹. The importance of subcellular localisation of autophagy regulators is also seen in *C. elegans*, where the RING ubiquitin ligase RPM-1, a PAM/Highwire/RPM-1 protein family homologous to mammalian Phr1/MYCBP2, spatially restricts UNC-51(ULK) degradation in neurons to inhibit autophagy⁷⁰. In the absence of *rpm-1*, excessive autophagy results in axonal and behavioural defects⁷⁰. Recently, variants in MYCBP2 have been identified in patients with a neurodevelopmental disorder⁷¹. Functional analysis of the variants using *C. elegans* model suggests that they increase axonal autophagosome formation and have defects in axon development and behaviour⁷¹. We propose that *detour* acts as a regulator of HOPS complex by promoting ubiquitination of HOPS subunits to tether the complex to the autophagy pathway. This highlights the critical role of tethering protein complexes to the appropriated compartment for the regulation of autophagic flux and that defects can have pathological consequences.

With dysregulation of autophagic flux identified in the pathology of many human diseases, including neurodegeneration and cancer, it is important to understand how this contributes to pathogenesis. The identification of *detour* in *Drosophila* and mammalian homologues ZNRF1 and ZNRF2 has provided the opportunity to define the role of the evolutionarily conserved membrane-associated RING E3 in autophagy in vivo. This study uncovers a function of the E3 *detour*, that interacts with HOPS complex and regulates autophagosome biogenesis.

Methods

***Drosophila* strains.** The midgut driver *Mex-GAL4* was obtained from Richard Burke (Monash University, Vic., Australia). The following stocks were from the Bloomington *Drosophila* Stock



Center (Bloomington, IN, USA): *w¹¹¹⁸ Mi{GFP[E.3xP3]=ET1} CG14435^{MB05816} (BL25464)*, *w¹¹¹⁸*; *sna^{Sc0}/SM6a*, *P{w[+mC]}=hsILMiT}2.4* (BL24613), *w¹¹¹⁸* (BL3605), *w¹¹¹⁸ Df(1)BSC297/Binsincy* (BL23681), *UAS-ZNRF1:HA* (BL79151), *UAS-ZNRF2* (BL86229), *GMR-GAL4* (BL1104), *UAS-lt RNAi* (BL34871), *UAS-Vps16A RNAi* (BL38271), *UAS-eGFP:Atg5* (BL59848), *UAS-GFP:LAMP1* (BL42714). The knockdown lines for *CG14435R-1*

(270R1), *UAS-dor RNAi* (3093R-2) and *UAS-lt RNAi* (18028R-2) were obtained from NIG-FLY, and *CG14435{GD8324}* (v17600), *UAS-Atg1 RNAi* from Vienna Drosophila RNAi Center. The *NPI-GAL4* (112001) and *UAS-Atg1^{GS10797}* (contains UAS regulatory sequences inserted upstream of the endogenous *Atg1* gene) lines were obtained from Kyoto Drosophila Genetic Resource Center. The *pmCherry-Atg8a* line expresses

Fig. 9 *detour* regulates autophagy and is required for healthy aging. **a** Immunoblot analysis of whole protein lysates from controls (w^{1118} and $detour^{rev}$), $detour^1$ and $detour^{MIET}$ young (Day 1) and old (Day 21) adults shows endogenous levels of ref(2)P and Atg8a. Actin (Act5C) as load control. **b** Quantitation of immunoblots demonstrating a significant increase in ref(2)P protein levels in young (Day 1) $detour^1$ and $detour^{MIET}$ adults. Data presented as mean relative intensity \pm SD ($n = 3$ individual repeat experiments; * $p < 0.05$, ** $p < 0.01$). **c** Adult brain section of a young (0-3d old male) control, $detour^1$ and $detour^{MIET}$ showing endogenous ref(2)P and Atg8a puncta. Scale bar = 20 μ m. **d** The transcript levels of selected AMP genes *Diptericin A* (*DptA*), *Drosocin* (*Dro*) and *Attacin-A* (*AttA*) from control (w^{1118}) and $detour$ mutant young (0-3 day, Day1) and old (Day 21) adults measured by qRT-PCR from total RNA with *rp49* as the reference gene. Data are from three/four independent experiments, each containing 3/5 adults per group (mean \pm SEM, * $p < 0.05$). **e** Survival assays for female control (w^{1118}/Df and $detour^{rev}/Df$), and $detour^1/Df$ and $detour^{MIET}/Df$ adults. Kaplan-Meier survival assay presented as percentage of surviving population per time point (Log-rank $p < 0.0001$; Gehan-Breslow-Wilcoxon $p < 0.0001$). **f** The percent of male flies unable to climb above 25 mm (climb defect) in a cylinder after 25 s was determined every week. Data presented as mean \pm SD, $n \geq 45$ flies per experiment (* $p < 0.05$; ** $p < 0.01$; **** $p < 0.0001$).

mCherry-tagged Atg8a from the endogenous *Atg8a* promoter, was used as a marker of autophagy⁴¹, and to generate mosaic clones *hsFLP*; *pmCherry-Atg8a*; *Act > CD2 > GAL4*, *UAS-nlsGFP/TM6B* line was used (from E. Baehrecke). Transgenic *UAS-detour-EGFP* lines were generated by BestGene Inc (CA, USA). The control was w^{1118} crossed to *Mex-GAL4*, or relevant driver line. The knockdown quantitation of the RNAi lines was determined by qRT-PCR from a minimum of 3/sample in triplicate. All flies were maintained and crossed performed at 25 °C unless otherwise stated, on *Drosophila* media [18.75% compressed yeast, 10% treacle, 10% polenta, 2.5% tegosept (10% parahydroxybenzoate in ethanol), 1.5% acid mix (47% proionic acid, 4.7% orthophosphoric acid) and 1% w/v agar].

Generation of the *detour*¹ mutant. An additional *detour* mutant allele was generated by mobilisation of a 7.5 kb *minos* transposable element within *detour*^{Mi} (w^{1118} *Mi{ET1}CG14435^{MB05816}*, marked by EGFP under *Pax6* promoter) by crossing to the *hsILMiT* transposase to produce lines with imprecise excisions affecting expression of the gene⁷². The mutant lines were identified by loss of EGFP expression in the eye and were crossed to w^{1118} for up to 6 generations to eliminate any off-target effects during this process. An excision event was identified in *detour* EGFP negative flies over *Df(1)BSC297* from single flies. The genomic deletions were determined by sequencing with specific primers spanning the insertion region. Briefly, genomic DNA was prepared from the *detour*¹ mutant and used as the template for PCR. Gel-purified PCR products were sequenced at SA Path. Sequences from the *CG4435*¹ mutant were compared to those from the parent X chromosome. A deletion was identified within intron 3 of putative *detour* transcript removing exon 4 and 5, which was designated as *detour* mutation 1 (w^{1118} , *detour*¹) (Fig. 2a). The *detour*^{rev} resulted from a precise excision.

Generation of constructs. Full-length *detour*, *lt*, and *V5* control gBlock® gene fragments (IDT) were cloned into the pENTR™/D-TOPO® or pENTR™/SD/D-TOPO® using the pENTR™ Directional TOPO® Cloning Kit (Invitrogen) according to the manufacturer's instructions. As *detour* contains a conserved motif for N-myristoylation, C-terminally tagged constructs were generated. To generate construct for expression in S2 cells, TOPO-*detour* and TOPO-*V5* were used to recombine inserts into the C-term EGFP tagged vector with Actin5C promoter, pAWG, destination vector (*Drosophila* Genomics Resource Center, #1072). A transformation construct for the *UAS-detour-EGFP* transgenic line was generated by insertion of TOPO-*detour* insert into in the C-term EGFP tagged P-element transformation vector, pTWG (Carnegie Institution for Science, *Drosophila* Gateway™ Vector Collection). Reactions were performed using the Gateway™ LR Clonase™ II Enzyme Mix (Invitrogen) according to the manufacturer's instructions. Full length *dor*, *lt* and *Vps16A* constructs

were generated by Gateway cloning into the pENTR™/D-TOPO® (Invitrogen) according to the manufacturer's instructions. The TOPO-*dor*, TOPO-*lt* and TOPO-*Vps16A* were used to recombine inserts into the appropriate tagged vector with Actin5C promoter, to generate pAFW-*dor* (FLAG-*dor*), pAMW-*Vps16A* (Myc-*Vps16A*), pAFW-*Vps16A* (Flag-*Vps16A*), pAHW-*lt* (HA-*lt*) and pAFW-*lt* (Flag-*lt*). Full length *detour* (TOTO-*detour*) was inserted in pIB-V5-His (RfB). Full-length ZNRF1 and ZNRF2 gBlock® gene fragment (IDT) were cloned into the pENTR™/D-TOPO® (Invitrogen) according to the manufacturer's instructions and used to recombine into pcDNA3.2 to generate ZNRF1:V5 and ZNRF2:V5 constructs. Reactions were performed using the Gateway™ LR Clonase™ II Enzyme Mix (Invitrogen) according to the manufacturer's instructions. The ubiquitin expression construct pIE4-HA-Ub was as described⁷³. gBlock® for *detour*, *lt*, ZNRF2 and *V5* were used for Gateway® cloning (Supplementary Table 1). Cloning primers (IDT) use are as follows: *dor* F 5'-caccATGGACACGTCTATGCCTAACC; R 5'-GTCTGAACGACGGTGGTAGC, *lt* F 5'-caccATGGCTAAAGCGTTGCCGCTC; R 5'-CGGGGTAACAGTTATGATGTCGC, *Vps16A* F 5'-caccATGCCTATCATGTACAACACGGGG; R 5'-AGCTTAAGAGTGC TATTCGTATAGAC.

Larval staging and midgut morphology analysis. Wandering third instar larvae raised on standard media supplemented with 0.05% bromophenol blue were transferred to a petri dish with moist Whatmann paper to monitor for gut clearance as visualized by loss of blue in the gut (-4 h RPF)⁷⁴. For morphological analysis, a minimum of 10 midguts were dissected in 1xPBS from appropriately aged animals fixed in 4% paraformaldehyde v/v in 1xPBS⁷⁵. Images were acquired using a stereo microscope (SZ61, Olympus, Tokyo, Japan) equipped with a 2x auxiliary objective (110AL 2x, Olympus) and digital camera (DP21, Olympus). To determine gastric caeca size, the gastric caeca was outlined with the magnetic lasso tool in Adobe Photoshop CS6 (Adobe, San Jose, CA, USA) and the number of pixels in this area was measured using the histogram function. The mean and SD. of gastric caeca size were calculated using Prism (GraphPad Software).

Live mCherry, eGFP and LysoTracker imaging. For live imaging of mCherry-Atg8a or eGFP-Atg5, a minimum of 10 midguts were dissected from appropriately staged animals in 1xPBS with Hoechst 33342 (2 μ g/ml, Sigma-Aldrich) to stain DNA and imaged immediately without fixation using a Zeiss confocal (LSM 800, Carl Zeiss Microscopy, Jena, Germany). The images were quantitated using ImageJ (Bethesda, MD, USA) to count puncta with a size >2 pixels and represented as the average puncta per cell. For LysoTracker staining, midguts were dissected in 1xPBS with 1 μ M LysoTracker Green DND26 (1:1000; Invitrogen Molecular Probes, L7526) and Hoechst 33342.

Immunostaining *Drosophila* tissue. Heads from animals of the required age were dissected and fixed with 4% v/v paraformaldehyde in 1xPBS at room temperature for 60 mins then washed for 60 mins in 1xPBTw (PBS + 0.1% tween) prior to overnight incubation in 30% sucrose in PBS on nutator at 4 °C. Tissues were embedded in OCT and stored at -80 until 14 micron sections cut. Tissue sections were then blocked with 1xPBS + 0.3% triton X + 1% BSA. For midgut tissue, animals of the required stages were dissected in 1xPBS and fixed with 4% v/v paraformaldehyde in 1xPBS at room temperature for 45 mins. Tissues were then washed 3 x 10 min 1xPBTx (PBS + 0.1% triton X) and blocked with 1xPBTx + 1% BSA at room temperature for 1 h. Samples were incubated with primary antibody in blocking buffer overnight at 4 °C. Primary antibodies were: rabbit anti-ref(2)P 1:500 (Abcam ab178440), rabbit anti-GABARAP 1:200 (referred to as Atg8a; Abcam ab109364), mouse anti-Rab7 1:10 (DSHB), rabbit anti-phospho-Akt 1:200 (Cell Signalling 4054) and goat anti-GFP 1:500 (Rockford 600-101-215). Following 4 x 30 min washes in 1xPBTx (PBS + 0.1% triton X), samples were incubated with secondary antibodies at room temperature for 1-2 h. Secondary antibodies: anti-rabbit Alexa-FLUOR 488, anti-rabbit Alexa-FLUOR 555, anti-mouse Alexa-FLUOR 488 or anti-mouse Alexa-FLUOR 647 (1:200, Molecular Probes, Eugene, CA, USA). Samples were washed 3 x 10 min in 1xPBTx, stained with Hoechst 33342 (2 µg/µL) for 1 min and mounted in ProLong® Gold Antifade (Thermo Scientific) or 80% glycerol/PBS and imaged on a Zeiss LSM 800 confocal microscope (Carl Zeiss Microscopy, Jena, Germany).

Confocal microscopy. Confocal images were obtained using a Carl Zeiss LSM 800 Axio Observer 7 confocal microscope with 405 nm (5 mW), 488 nm (10 mW), 561 nm (10 mW) and 640 nm (5 mW) lasers visualized with PlanApo 40x/1.3 or 63x/1.4 Oil DIC objectives (Carl Zeiss Microscopy, Jena, Germany). Images captured by Zen 2011 (Black Edition) software (Carl Zeiss Microscopy) were exported into Photoshop (Adobe, San Jose, CA, USA).

Transmission electron microscopy. Midguts from appropriately staged larvae were dissected in 1xPBS then fixed in 1.25% glutaraldehyde, 4% sucrose, 4% paraformaldehyde in PBS for 30 min at room temperature. Samples were then washed with 4% sucrose in PBS, post-fixed in 1% osmium tetroxide for 1 h, dehydrated, treated with propylene oxide, and infiltrated for embedding in resin⁷⁵. Ultrathin sections were cut on grids, stained for 2 min with 4% uranyl acetate in 25% ethanol and 2 min in Reynold's lead citrate before examination using Tecnai G2 Spirit TEM (Adelaide Microscopy).

Lifespan assay. Newly eclosed flies (D0-3) were collected in groups of 20 per vial with a minimum of four replicates per genotype and maintained at 29 °C. They were transferred to fresh medium every 2-3 days and deaths recorded. Each experiment was repeated at least two times. Kaplan-Meier curves and statistical analysis was performed according to Prism survival function, with a log-rank Mantel-Cox test to determine statistical significance.

Climbing assay. Locomotor decline during aging was monitored by conducting climbing assay. Briefly, without anaesthetization, 2 x 15 male flies of respective genotype were transferred into 500 mL measuring cylinders, each containing 15 flies. The top of the cylinder was sealed with parafilm to prevent flies escaping. The cylinder was gently tapped three times to bring the flies down to the bottom and the number of flies that climb up within each predefined area of the cylinder (<50 mL = 25 mm, >300 mL =

160 mm) after 25 s was recorded. This assay was performed weekly from day 1 post-eclosion to day 21 age. Three replicates were conducted for each cohort ($n = 15$) of flies and were allowed 2 min reset before tapping down and 1 min between each assay.

S2 cell culture and transfection. S2 cells were cultured in complete Schneider's medium in a 28 °C humidified incubator (Sanyo) and passaged twice a week at 1:2-1:4 dilutions. For each transfection, 52.5 µL of Cellfectin® II transfection reagent (Invitrogen), 7 µg of plasmid DNA and 42 µL of PLUS™ reagent (Invitrogen) were diluted in 550 µL of Schneider's medium and incubated for 5 min at room temperature. The diluted plasmid DNA and diluted Cellfectin® II reagents were combined and incubated for 20 min at room temperature. The cell medium was replaced with 5 mL of plasmid DNA-Cellfectin® II mixture resuspended in Schneider's medium. Cells were incubated in a 28 °C humidified incubator (Sanyo) for 4 h before adding 5 mL of Schneider's medium supplemented with 20% FCS. Transfected cells were harvested for protein extraction 48 h post-transfection.

ZNRF1-V5 and ZNRF2-V5 transfections. 4×10^5 HeLa cells were transfected with 2 µg of plasmid using Lipofectamine 3000 according to manufacturer's instructions. 24 h post-transfection, cells were lysed in 30 µL of ice-cold NP-40-containing lysis buffer and 20 µL processed for immunoblotting as below.

Immunostaining cells. HeLa cells were grown in DMEM media (Gibco) supplemented with 10% FBS, 2mM L-glutamine, 100 µM penicillin/streptomycin and HEPES. Cells were plated on glass coverslips overnight at 2×10^5 cells/mL and fixed for 20 min in 4% v/v paraformaldehyde in 1xPBS at room temperature, then incubated with 1xPBTx for 10 min. Cells were washed 3 times in 1xPBS and blocked for 30 min with blocking buffer (1% BSA, 1% goat serum in PBS). The blocking buffer was removed and primary antibodies, anti-Sequestosome 1 (SQSTM1/p62) (Abnova H00008878-M01 Mouse; 1:200), anti-GABARAPs (Abcam ab109364 Rabbit; 1:200) or anti-V5 (Abcam 27671 Mouse 1:200), incubated at room temperature for 2 h. Cells were then washed 3 times in 1xPBS. The AlexaFluor-488 (1:200) secondary antibody was incubated at room temperature for 1 h. Cells were then washed 3 times in 1xPBS and counterstained with Hoechst 33342 and mounted in Prolong Gold Antifade. For chloroquine treatment, 200 µM of chloroquine was added for 4 h prior to staining.

LysoTracker and magic red staining. HeLa cells were grown as for immunostaining. For LysoTracker staining, cells were incubated in 1xPBS with 1 µM LysoTracker Green DND26 (1:1000; Invitrogen Molecular Probes, L7526 respectively) and Hoechst 33342 for 5 min then washed in 1xPBS and imaged immediately. The Magic Red staining was performed according to manufactures protocol, Cathepsin L Assay Kit (Magic Red) (ab270774). For fluorescence plate reader analysis of Magic Red, cells were plated in triplicate in a 96-well flat bottom transparent plate according to manufactures protocol and fluorescence readings were recorded using a microplate reader Spark 10 M with SparkControl Magellan (Tecan Group Ltd., Männedorf, Switzerland).

Generation of ZNRF1 and ZNRF2 KO HeLa cell lines. ZNRF1 and ZNRF2 KO HeLa cell lines were generated using CRISPR-Cas9 technology⁷⁶. The small guide RNAs (sgRNAs) targeting a region in exon 1 of human ZNRF1 and ZNRF2, respectively, were cloned into the pSpCas9(BB)-2A-Puro (PX459) vector plasmid (a gift from Feng Zhang; Addgene plasmid # 48139;

<http://n2t.net/addgene:48139>; RRID:Addgene_48139). The following sgRNA oligos (IDT) were used:

ZNRF1: Sense 5'-CACCGTCTCTGGTAACCATTGCCAT
Anti-sense 5'-AAACATGGCAATGGTTACCAGGAGC,
ZNRF2: Sense 5'-CACCGAGCCCGAGTACGCGCGCGTG
Anti-sense 5'-AAACCACGCGCGCTACTCGGGCTC

The plasmid was transfected using Lipofectamine 3000 reagent (Invitrogen), with an empty PX459 vector serving as a control to generate wild type clones. After 24 h, media was replaced and supplemented with 2.5 µg/mL puromycin (Sigma-Aldrich) for a further 24 h to select for transfected cells. Surviving cells were passaged at low seeding density and single colonies selected and propagated. To screen candidate single clones for both *ZNRF1* KO (B8), *ZNRF2* KO (D9) and control wild type (W6) (empty PX459 vector), the sgRNA-bound area was amplified by PCR with following primers:

ZNRF1 F 5'-TGCTGCTGAGAAGTGGGGGAG; R 5'-CTAGTTTCCAGACGGTAGGTATC, ZNRF2 F 5'-ACCA-GAACCGAAACCAGCG; R 5'-GCTG GGCACCTGAGCC.

The PCR products were run on 2% agarose gel and purified with QIAquick Gel extraction Kit (Qiagen) according to the manufacturer's instruction and were subjected to DNA sequencing. DNA sequencing results were used for insertion and deletion analysis in the targeted gene area by TIDE software (<http://tide.nki.nl>) and alignment by ClustalW software (<https://www.genome.jp/tools-bin/clustalw>). Loss of *ZNRF1* and *ZNRF2* expression was validated by qPCR and /or Western blot.

Quantitative real time PCR (qRT-PCR). Total RNA was isolated from cells, whole flies or midguts dissected from appropriately staged animals using TRIzol® reagent (Life Technologies, Carlsbad, CA) according to the manufacturer's instructions. cDNA synthesis was performed using the High Capacity cDNA Reverse Transcription Kit (Applied Biosciences) with 1 µg of RNA, random primers and RNaseOUT™ Recombinant Ribonuclease Inhibitor (Thermo Fisher) according to the manufacturer's instructions. qRT-PCR was performed using KAPA SYBR® FAST according to manufacturer's instructions on a Rotor-Gene Q (Qiagen, Valencia, CA, USA) controlled with Rotor-Gene software. Reactions were performed in triplicate and normalised gene expression was calculated relative to that of control gene (*rp49*, also known as *rpL32*, for *Drosophila* and *β-actin* for human) using standard curves in Q-Gene software. Primers used for qRT-PCR from IDT, except *detour* and *dor* from GeneWorks (Supplementary Table 2).

Protein extraction. Transfected S2 cells were centrifuged at 2000 rpm for 2 min at room temperature and resuspended in 1 mL of 1xPBS. These pellets were either resuspension in 500 µL of ice-cold NP-40-containing lysis buffer containing Halt™ complete protease/phosphatase single-use inhibitor cocktail (Thermo Scientific) and 0.5 M EDTA (Thermo Scientific). Protein was then extracted by probe sonication using an ultrasonic liquid processor (Vibra-Cell™ VCX 130) equipped with a 1/8th inch stepped microtip (Sonic) for a total sonication time of 30 s (Amp: 1 50%, ON:10 s, OFF: 10 s, ON: 10 s). Lysates were centrifuged at 13,200 rpm for 10 min at 4 °C to pellet debris and the remaining lysates were transferred to new microcentrifuge tubes.

GFP Immunoprecipitation. 150 µL of GFP-Trap®_MA bead slurry (Chromotek) per immunoprecipitation was equilibrated by washing three times with 1 mL of ice-cold NP-40-containing lysis buffer. 15 µL and 20 µL of lysate were reserved as the input for mass-spectrometry (MS) and immunoblot analysis respectively, while the remaining lysates were added to the equilibrated beads

and left overnight at 4 °C on a nutator. The beads were then briefly centrifuged in a microcentrifuge and the supernatant was collected for immunoblot analysis. The beads were washed three times in 1 mL of ice-cold NP-40-containing lysis buffer followed by a final wash in 1 mL of lysis buffer without NP-40 to remove the detergent. Any residual lysis buffer was removed by briefly centrifuging in a microcentrifuge. Proteins were then eluted by adding 50 µL of 0.2 M glycine (pH 2.5) for 2 min with constant mixing by gently flicking the tubes. Eluates were transferred to new microcentrifuge tubes and neutralised with 5 µL of 1 M Tris-HCl (pH 10.4). The elution and neutralisation steps were performed three times.

Endogenous immunoprecipitation. HeLa cells harvested from a confluent T75 flask were lysed in 500 µL ice-cold NP-40-containing lysis buffer. 50 µL of lysate was reserved as the input, and the remaining lysates were precleared for 30 min at 4 °C with magnetic protein G-Sepharose (Amersham Biosciences). Precleared samples were incubated with 10 µL of magnetic protein G-Sepharose beads and 1 µL of either rabbit anti-ZNRF2 (Novus Biologicals NBP1-28715), rabbit anti-VPS18 (Abclonal A16654) or rabbit anti-IgG. The protein-bound beads were then washed twice in lysis buffer and once in PBS, boiled at 95 °C for 5 min and run on 10% SDS-PAGE gels for immunoblotting as below.

For the detection VPS18 ubiquitination, parental (W6), *ZNRF1* KO (B8) and *ZNRF2* KO (D9) HeLa cells were incubated with 10 µM MG132 (Sigma-Aldrich) for 4 h. The cells were lysed in 100 µL cell lysis buffer (2% SDS, 150 mM NaCl, 10 mM Tris-HCl, Ph 8.0) in a 1.5 ml tube, followed by incubation at 95 °C for 10 min. Next, 900 µL dilution buffer (10 mM Tris-HCl, 150 mM NaCl, 2 mM EDTA, 1% Triton X-100, Ph 8.0) was added, followed by sonication. The diluted samples were spun at 15,000 rpm for 20 min at 4 °C. The supernatant was mixed with protein A/G beads and rabbit anti-VPS18 antibody (Abclonal A17563) in a 1.5 ml tube and incubated overnight at 4 °C with rotation. After four times wash as described above, the beads were boiled in 40 µL 2 x SDS loading buffer for immunoblotting.

Detection of protein ubiquitination in cultured S2 cells.

Transfected S2 cells were lysed with 100 µL cell lysis buffer (2% SDS, 150 mM NaCl, 10 mM Tris-HCl, pH 8.0) in a 1.5 ml tube and heated for 10 min at 100 °C, followed by sonication. After sonication, 900 µL dilution buffer (10 mM Tris-HCl, pH 8.0, 150 mM NaCl, 2 mM EDTA, 1% Triton) was added and the diluted samples were spun at 15,000 rpm for 20 min at 4 °C. The supernatant was transferred to a new tube. Protein G/A agarose magnet beads (Thermo Fischer) were equilibrated with dilution buffer. The cell lysate, protein G/A beads and rabbit anti-HA antibody were mixed and incubated overnight at 4 °C with rotation. The tubes were placed on a magnet stand and the supernatant was aspirated. The protein G/A beads were washed with dilution buffer four times. After the last wash, the beads were boiled with 2 x SDS loading buffer and subjected to immunoblotting.

Immunoblotting. To denature proteins for SDS-PAGE, 10 µL of protein lysates were boiled in protein loading buffer for 4 min and centrifuged at 13,000 rpm for 1 min. Prepared samples were run on a 15-well 4-15% Mini-PROTEAN® TGX™ Stain-Free™ pre-cast polyacrylamide gel (Bio-Rad, Hercules, CA, USA) for 1 h at 110 V in SDS-PAGE running buffer (250 mM Tris, 192 mM glycine, 0.06% SDS). The proteins were transferred onto PVDF or nitrocellulose membrane (Bio-Rad) using a Trans-Blot Turbo (Bio-Rad), for 30 min at 25 V in transfer buffer (25 mM Tris,

192 mM glycine, 20% methanol, 0.05% SDS) according to the manufacturer's instructions. Membranes were blocked with 5% w/v skim milk (Diploma) in TBST blocking buffer [TBST (20 mM Tris, 150 mM NaCl pH 7.4, 0.05% Tween- 20)], for 1 h at room temperature. Membranes were incubated overnight with anti-GFP (Rockford 600-101-215 Goat 1:500), anti-HA (Cell Signaling CST.2367 S (6E2) Mouse 1:500), anti-FLAG (Sigma F1804 Mouse 1:500), anti-Myc (NEB 2276 S (9B11) Mouse 1:500), anti-Microtubule-associated protein 1 light chain 3 (LC3B) (Novus Biologicals 100-2220 Rabbit 1:200), anti-Sequestosome 1 (SQSTM1/p62) (Abnova H00008878-M01 Mouse 1:200), anti-ZNRF2 (Novus NBP1-28715 Rabbit 1:500), anti-V5 (Abcam ab27671 Mouse 1:500), anti-VPS18 (Abclonal A16654 Rabbit 1:500), anti-VPS18 (Abclonal A17563, Rabbit 1:1000), anti-Ubiquitin-horseradish peroxidase (HRP) (Santa Cruz sc-8017 Mouse 1:500), anti-Cathepsin L/MEP (Abcam ab58991 Rabbit 1:500) or anti-Act5C/ACTB/ β -actin (Sigma Aldrich A1978 Mouse), diluted in blocking buffer at 4 °C with rocking. Membranes were washed 4×15 min with TBST before incubation with anti-goat horseradish peroxidase (HRP) (1:20,000), also diluted in blocking buffer, for 1 h at room temperature with rocking. Membranes were then washed 4×10 min with TBST then developed using ECL™ Prime Western Blotting Detection Reagent (GE Healthcare) and imaged using the ImageQuant LAS 4000 and Typhoon FLA 9000 (GE Healthcare).

Mass spectrometry. GFP-Trap protein samples were resuspended in 6 M Urea, 100 mM DTT and 100 mM Tris-HCl pH 7.0, and subjected to protein digestion using a FASP column (Expedeon Inc.)⁷⁷. Peptides were lyophilised to dryness, resuspended in 2% ACN and 1% FA before injection and separation by reversed-phase liquid chromatography on an M-class ultra-high performance liquid chromatography (UHPLC) system (Waters) using a 250 mm × 75 μ m column (1.6 μ m C18, packed emitter tip; Ion Opticks) with a linear 90-min gradient at a flow rate of 400 nL/min from 98% solvent A (0.1% FA in Milli-Q water) to 35% solvent B (0.1% FA, 99.9% ACN). The nano-UHPLC was coupled on-line to an Impact II mass spectrometer equipped with a CaptiveSpray ionization source (Bruker Daltonics) and column oven at 40 °C (Sonation). The Impact II was operated in a data-dependent mode using a 1.5 s cycle time, switching automatically between one full-scan (4 Hz) and subsequent MS/MS scans for the remaining time with spectra rate determined using peptide intensity. The raw files were analysed using the MaxQuant software^{78,79} version 1.5.8. The database search was performed using *D. melanogaster* protein sequences obtained from UniProt.

Bioinformatics. The obtained Universal Protein Knowledgebase (UniProt v2.16; <http://www.uniprot.org>)⁸⁰ accession numbers were processed through Database for Annotation, Visualization & Integrated Discovery (DAVID) bioinformatics resources v.6.7 (<https://david.ncifcrf.gov/>)^{81,82} and Kyoto Encyclopaedia of Genes and Genomes (KEGG) pathway maps database (<http://www.genome.jp/kegg>)^{83,84}. For all enrichment analyses, a Benjamini–Hochberg corrected *p*-value ≤ 0.05 was considered strongly enriched.

Statistics and reproducibility. All survival data were analysed by Kaplan–Meier Log-rank Test for overall survival and by the Student's *t*-test for mean and maximum lifespan using Graph Pad Prism. Other comparisons were determined either by Student's *t*-test or One-way ANOVA followed by post hoc *t*-test or Fisher's LSD test, with *p* < 0.05 considered statistically significant.

Reporting summary. Further information on research design is available in the Nature Portfolio Reporting Summary linked to this article.

Data availability

The mass spectrometry proteomics data have been deposited to the ProteomeXchange Consortium via the PRIDE⁸⁵ partner repository with the dataset identifier PXD036857. The data that support the findings of this study are available in Supplementary Data 1. The uncropped and unedited blots/gels are shown in Supplementary Figs. 8–13, in the Supplementary Information.

Received: 14 December 2023; Accepted: 18 January 2024;

Published online: 15 February 2024

References

- Galluzzi, L. et al. Molecular definitions of autophagy and related processes. *EMBO J.* **36**, 1811–1836 (2017).
- Dikic, I. & Elazar, Z. Mechanism and medical implications of mammalian autophagy. *Nat. Rev. Mol. Cell Biol.* **19**, 349 (2018).
- Levine, B. & Kroemer, G. Biological functions of autophagy genes: a disease perspective. *Cell* **176**, 11–42 (2019).
- Aman, Y. et al. Autophagy in healthy aging and disease. *Nat Aging* **1**, 634–650 (2021).
- Klionsky, D. J. et al. Autophagy in major human diseases. *EMBO J.* **40**, e108863 (2021).
- Komatsu, M. et al. Loss of autophagy in the central nervous system causes neurodegeneration in mice. *Nature* **441**, 880–884 (2006).
- Hara, T. et al. Suppression of basal autophagy in neural cells causes neurodegenerative disease in mice. *Nature* **441**, 885–889 (2006).
- O'Keefe, L. & Denton, D. Using *Drosophila* models of amyloid toxicity to study autophagy in the pathogenesis of Alzheimer's disease. *Biomed. Res. Int.* **2018**, 5195416 (2018).
- Varga, K. et al. Loss of Atg16 delays the alcohol-induced sedation response via regulation of Corazonin neuropeptide production in *Drosophila*. *Sci. Rep.* **6**, 34641 (2016).
- Kim, M. et al. Mutation in ATG5 reduces autophagy and leads to ataxia with developmental delay. *Elife* **5**, e12245 (2016).
- Kim, M. et al. *Drosophila* Fip200 is an essential regulator of autophagy that attenuates both growth and aging. *Autophagy* **9**, 1201–1213 (2013).
- Juhász, G., Erdi, B., Sass, M. & Neufeld, T. P. Atg7-dependent autophagy promotes neuronal health, stress tolerance, and longevity but is dispensable for metamorphosis in *Drosophila*. *Genes Dev.* **21**, 3061–3066 (2007).
- Simonsen, A. et al. Promoting basal levels of autophagy in the nervous system enhances longevity and oxidant resistance in adult *Drosophila*. *Autophagy* **4**, 176–184 (2008).
- Pyo, J. O. et al. Overexpression of Atg5 in mice activates autophagy and extends lifespan. *Nat. Commun.* **4**, 2300 (2013).
- Yu, S. & Melia, T. J. The coordination of membrane fission and fusion at the end of autophagosome maturation. *Curr. Opin. Cell Biol.* **47**, 92–98 (2017).
- Jiang, P. et al. The HOPS complex mediates autophagosome-lysosome fusion through interaction with syntaxin 17. *Mol. Biol. Cell* **25**, 1327–1337 (2014).
- Balderhaar, H. J. & Ungermann, C. CORVET and HOPS tethering complexes - coordinators of endosome and lysosome fusion. *J. Cell Sci.* **126**, 1307–1316 (2013).
- van der Beek, J., Jonker, C., van der Welle, R., Liv, N. & Klumperman, J. CORVET, CHEVI and HOPS—multisubunit tethers of the endo-lysosomal system in health and disease. *J. Cell Sci.* **132**, jcs189134 (2019).
- Pols, M. S., ten Brink, C., Gosavi, P., Oorschot, V. & Klumperman, J. The HOPS proteins hVps41 and hVps39 are required for homotypic and heterotypic late endosome fusion. *Traffic* **14**, 219–232 (2013).
- Takats, S. et al. Interaction of the HOPS complex with Syntaxin 17 mediates autophagosome clearance in *Drosophila*. *Mol. Biol. Cell* **25**, 1338–1354 (2014).
- Wartosch, L., Gunesdogan, U., Graham, S. C. & Luzio, J. P. Recruitment of VPS33A to HOPS by VPS16 Is required for lysosome fusion with endosomes and autophagosomes. *Traffic* **16**, 727–742 (2015).
- Zhen, Y. & Li, W. Impairment of autophagosome-lysosome fusion in the buff mutant mice with the VPS33A(D251E) mutation. *Autophagy* **11**, 1608–1622 (2015).
- van der Welle, R. E. N. et al. Neurodegenerative VPS41 variants inhibit HOPS function and mTORC1-dependent TFEB/TFE3 regulation. *EMBO Mol. Med.* **13**, e13258 (2021).
- Grumati, P. & Dikic, I. Ubiquitin signaling and autophagy. *J. Biol. Chem.* **293**, 5404–5413 (2018).

25. Yin, Z., Popelka, H., Lei, Y., Yang, Y. & Klionsky, D. J. The roles of ubiquitin in mediating autophagy. *Cells* **9**, 2025 (2020).
26. Di Rienzo, M. et al. Autophagy induction in atrophic muscle cells requires ULK1 activation by TRIM32 through unanchored K63-linked polyubiquitin chains. *Sci. Adv.* **5**, eaau8857 (2019).
27. Nazio, F. et al. mTOR inhibits autophagy by controlling ULK1 ubiquitylation, self-association and function through AMBRA1 and TRAF6. *Nat. Cell Biol.* **15**, 406–416 (2013).
28. Shi, C. S. & Kehrl, J. H. TRAF6 and A20 regulate lysine 63-linked ubiquitination of Beclin-1 to control TLR4-induced autophagy. *Sci. Signal* **3**, ra42 (2010).
29. Xia, P. et al. WASH inhibits autophagy through suppression of Beclin 1 ubiquitination. *EMBO J.* **32**, 2685–2696 (2013).
30. Antonioni, M. et al. AMBRA1 interplay with cullin E3 ubiquitin ligases regulates autophagy dynamics. *Dev. Cell* **31**, 734–746 (2014).
31. Liu, C. C. et al. Cul3-KLHL20 ubiquitin ligase governs the turnover of ULK1 and VPS34 complexes to control autophagy termination. *Mol. Cell* **61**, 84–97 (2016).
32. Denton, D. et al. Autophagy, not apoptosis, is essential for midgut cell death in *Drosophila*. *Curr. Biol.* **19**, 1741–1746 (2009).
33. Xu, T., Nicolson, S., Denton, D. & Kumar, S. Distinct requirements of autophagy-related genes in programmed cell death. *Cell Death Differ.* **22**, 1792–1802 (2015).
34. Chang, T.-K. et al. Uba1 functions in Atg7- and Atg3-independent autophagy. *Nat. Cell Biol.* **15**, 1067–1078 (2013).
35. Hoxhaj, G. et al. The E3 ubiquitin ligase ZNRF2 is a substrate of mTORC1 and regulates its activation by amino acids. *Elife* **5**, e12278 (2016).
36. Araki, T., Nagarajan, R. & Milbrandt, J. Identification of genes induced in peripheral nerve after injury. Expression profiling and novel gene discovery. *J. Biol. Chem.* **276**, 34131–34141 (2001).
37. Araki, T. & Milbrandt, J. ZNRF proteins constitute a family of presynaptic E3 ubiquitin ligases. *J. Neurosci.* **23**, 9385–9394 (2003).
38. Wakatsuki, S., Saitoh, F. & Araki, T. ZNRF1 promotes wallerian degeneration by degrading AKT to induce GSK3B-dependent CRMP2 phosphorylation. *Nat. Cell Biol.* **13**, 1415–1423 (2011).
39. Denton, D. & Kumar, S. Autophagy-dependent cell death. *Cell Death Differ.* **26**, 605–616 (2019).
40. Jiang, C., Baehrecke, E. H. & Thummel, C. S. Steroid regulated programmed cell death during *Drosophila* metamorphosis. *Development* **124**, 4673–4683 (1997).
41. Denton, D. et al. Relationship between growth arrest & autophagy in midgut programmed cell death in *Drosophila*. *Cell Death Differ.* **19**, 1299–1307 (2012).
42. Scott, R. C., Schuldiner, O. & Neufeld, T. P. Role and regulation of starvation-induced autophagy in the *Drosophila* fat body. *Dev. Cell* **7**, 167–178 (2004).
43. Mizushima, N., Yoshimori, T. & Ohsumi, Y. The role of Atg proteins in autophagosome formation. *Annu. Rev. Cell Dev. Biol.* **27**, 107–132 (2011).
44. Mauvezin, C., Ayala, C., Braden, C. R., Kim, J. & Neufeld, T. P. Assays to monitor autophagy in *Drosophila*. *Methods* **68**, 134–139 (2014).
45. Scott, R. C., Juhasz, G. & Neufeld, T. P. Direct induction of autophagy by Atg1 inhibits cell growth and induces apoptotic cell death. *Curr. Biol.* **17**, 1–11 (2007).
46. Nakatogawa, H. et al. The autophagy-related protein kinase Atg1 interacts with the ubiquitin-like protein Atg8 via the Atg8 family interacting motif to facilitate autophagosome formation. *J. Biol. Chem.* **287**, 28503–28507 (2012).
47. Wang, C. et al. Phosphorylation of ULK1 affects autophagosome fusion and links chaperone-mediated autophagy to macroautophagy. *Nat. Commun.* **9**, 3492 (2018).
48. Hoxhaj, G. et al. ZNRF2 is released from membranes by growth factors and, together with ZNRF1, regulates the Na⁺/K⁺ATPase. *J. Cell Sci.* **125**, 4662–4675 (2012).
49. Shen, C. H. et al. ZNRF1 mediates epidermal growth factor receptor ubiquitination to control receptor lysosomal trafficking and degradation. *Front. Cell Dev. Biol.* **9**, 642625 (2021).
50. Li, Z. & Blissard, G. The vacuolar protein sorting genes in insects: a comparative genome view. *Insect Biochem. Mol. Biol.* **62**, 211–225 (2015).
51. Segala, G. et al. Vps11 and Vps18 of Vps-C membrane traffic complexes are E3 ubiquitin ligases and fine-tune signalling. *Nat. Commun.* **10**, 1833 (2019).
52. Berry, D. L. & Baehrecke, E. H. Growth arrest and autophagy are required for salivary gland cell degradation in *Drosophila*. *Cell* **131**, 1137–1148 (2007).
53. Nagy, P., Varga, A., Kovacs, A. L., Takats, S. & Juhasz, G. How and why to study autophagy in *Drosophila*: it's more than just a garbage chute. *Methods* **75**, 151–161 (2015).
54. Nezis, I. P. et al. Ref(2)P, the *Drosophila melanogaster* homologue of mammalian p62, is required for the formation of protein aggregates in adult brain. *J. Cell Biol.* **180**, 1065–1071 (2008).
55. Richards, R. I. et al. The Enemy within: innate surveillance-mediated cell death, the common mechanism of neurodegenerative disease. *Front. Neurosci.* **10**, 193 (2016).
56. Wu, J., Randle, K. E. & Wu, L. P. Ird1 is a Vps15 homologue important for antibacterial immune responses in *Drosophila*. *Cell. Microbiol.* **9**, 1073–1085 (2007).
57. Shukla, A. K., Spurrier, J., Kuzina, I. & Giniger, E. Hyperactive innate immunity causes degeneration of dopamine neurons upon altering activity of Cdk5. *Cell. Rep.* **26**, 131–144.e134 (2019).
58. Tusco, R. et al. Kenny mediates selective autophagic degradation of the IKK complex to control innate immune responses. *Nat. Commun.* **8**, 1264 (2017).
59. Kishi-Itakura, C., Koyama-Honda, I., Itakura, E. & Mizushima, N. Ultrastructural analysis of autophagosome organization using mammalian autophagy-deficient cells. *J. Cell. Sci.* **127**, 4089–4102 (2014).
60. Sou, Y. S. et al. The Atg8 conjugation system is indispensable for proper development of autophagic isolation membranes in mice. *Mol. Biol. Cell.* **19**, 4762–4775 (2008).
61. Uemura, T. et al. A cluster of thin tubular structures mediates transformation of the endoplasmic reticulum to autophagic isolation membrane. *Mol. Cell. Biol.* **34**, 1695–1706 (2014).
62. Tsuboyama, K. et al. The ATG conjugation systems are important for degradation of the inner autophagosomal membrane. *Science* **354**, 1036–1041 (2016).
63. Plans, V. et al. The RING finger protein RNF8 recruits UBC13 for lysine 63-based self polyubiquitylation. *J. Cell. Biochem.* **97**, 572–582 (2006).
64. Behera, A. P. et al. Structural insights into the nanomolar affinity of RING E3 ligase ZNRF1 for Ube2N and its functional implications. *Biochem. J.* **475**, 1569–1582 (2018).
65. Shin, M. E., Ogburn, K. D., Varban, O. A., Gilbert, P. M. & Burd, C. G. FYVE domain targets Pib1p ubiquitin ligase to endosome and vacuolar membranes. *J. Biol. Chem.* **276**, 41388–41393 (2001).
66. Renz, C. et al. Ubc13-Mms2 cooperates with a family of RING E3 proteins in budding yeast membrane protein sorting. *J. Cell. Sci.* **133**, jcs244566 (2020).
67. Gu, C. et al. ZNRF2 attenuates focal cerebral ischemia/reperfusion injury in rats by inhibiting mTORC1-mediated autophagy. *Exp. Neurol.* **342**, 113759 (2021).
68. Ferrari, V. et al. Valosin containing protein (VCP): a multistep regulator of autophagy. *Int. J. Mol. Sci.* **23**, 1939 (2022).
69. Johnson, A. E. et al. SVIP is a molecular determinant of lysosomal dynamic stability, neurodegeneration and lifespan. *Nat. Commun.* **12**, 513 (2021).
70. Crawley, O. et al. Autophagy is inhibited by ubiquitin ligase activity in the nervous system. *Nat. Commun.* **10**, 5017 (2019).
71. AlAbdi, L. et al. Loss-of-function variants in MYCBP2 cause neurobehavioural phenotypes and corpus callosum defects. *Brain* **146**, 1373–1387 (2023).
72. Metaxakis, A., Oehler, S., Klinakis, A. & Savakis, C. Minos as a genetic and genomic tool in *Drosophila melanogaster*. *Genetics* **171**, 571–581 (2005).
73. Dalton, H. E. et al. *Drosophila* Ndfip is a novel regulator of Notch signaling. *Cell Death Differ.* **18**, 1150–1160 (2011).
74. Denton, D., Mills, K. & Kumar, S. Methods and protocols for studying cell death in *Drosophila*. *Methods Enzymol.* **446**, 17–37 (2008).
75. Xu, T., Kumar, S. & Denton, D. Characterization of autophagic responses in *Drosophila melanogaster*. *Methods Enzymol.* **588**, 445–465 (2017).
76. Ran, F. A. et al. Genome engineering using the CRISPR-Cas9 system. *Nat. Protoc.* **8**, 2281–2308 (2013).
77. Wisniewski, J. R., Zougman, A., Nagaraj, N. & Mann, M. Universal sample preparation method for proteome analysis. *Nat. Methods* **6**, 359–362 (2009).
78. Cox, J. & Mann, M. MaxQuant enables high peptide identification rates, individualized p.p.b.-range mass accuracies and proteome-wide protein quantification. *Nat. Biotechnol.* **26**, 1367–1372 (2008).
79. Cox, J. et al. Andromeda: a peptide search engine integrated into the MaxQuant environment. *J. Proteome Res.* **10**, 1794–1805 (2011).
80. UniProt, C. UniProt: a hub for protein information. *Nucleic Acids Res.* **43**, D204–212 (2015).
81. Huang da, W., Sherman, B. T. & Lempicki, R. A. Systematic and integrative analysis of large gene lists using DAVID bioinformatics resources. *Nat. Protoc.* **4**, 44–57 (2009).
82. Huang da, W., Sherman, B. T. & Lempicki, R. A. Bioinformatics enrichment tools: paths toward the comprehensive functional analysis of large gene lists. *Nucleic Acids Res.* **37**, 1–13 (2009).
83. Kanehisa, M. & Goto, S. KEGG: kyoto encyclopedia of genes and genomes. *Nucleic Acids Res.* **28**, 27–30 (2000).
84. Kanehisa, M. et al. Data, information, knowledge and principle: back to metabolism in KEGG. *Nucleic Acids Res.* **42**, D199–205 (2014).
85. Perez-Riverol, Y. et al. The PRIDE database and related tools and resources in 2019: improving support for quantification data. *Nucleic Acids Res.* **47**, D442–D450 (2019).

Acknowledgements

This work was supported by a National Health & Medical Research Council (NHMRC) of Australia Project Grant (1124490) to S.K. and D.D., as well as an Australian Research Council Discovery Project Grant (DP210100665), a University of South Australia

Support Package, a NHMRC Senior Principal Research Fellowship (GNT1103006) and a NHMRC L3 Investigator Grant (2007739) to S.K. S.N. was supported by a Research Training Program scholarship. Imaging facility at the Centre for Cancer Biology was established with funding from Australian Cancer Research Foundation (ACRF). We thank the Australian *Drosophila* Research Support Facility (Monash University, Vic., Australia), Vienna *Drosophila* Resource Center, and Bloomington *Drosophila* Stock Center for *Drosophila* stocks. The Rab7 monoclonal antibody was deposited by S. Munro to the Developmental Studies Hybridoma Bank, created by the NICHD of the NIH and maintained at The University of Iowa, Department of Biology, Iowa City, IA 52242. We thank the TRiP at Harvard Medical School (NIH/NIGMS R01-GM084947) for providing transgenic RNAi fly stocks. We thank Chris Leigh from Adelaide Microscopy (The University of Adelaide, Australia) for TEM sample preparation and microscopy.

Author contributions

D.D. and S.K. conceptualized and designed the project; D.D., S.N., J.M., Y.L., X.J., E.K., S.D., R.U., T.X. and J.S. performed experimental work; D.D., S.N., J.M., Y.L., X.J., E.K., S.D., R.U., T.X., J.S., A.W. and S.K. analyzed data; D.D. prepared the manuscript; S.K., D.D. and A.W. procured funding. All authors discussed the results and commented on the manuscript.

Competing interests

The authors declare no competing interest regarding the publication of this paper.

Additional information

Supplementary information The online version contains supplementary material available at <https://doi.org/10.1038/s42003-024-05834-1>.

Correspondence and requests for materials should be addressed to Sharad Kumar or Donna Denton.

Peer review information This manuscript has been previously reviewed at another Nature Portfolio journal. The manuscript was considered suitable for publication without further review at Communications Biology.

Reprints and permission information is available at <http://www.nature.com/reprints>

Publisher's note Springer Nature remains neutral with regard to jurisdictional claims in published maps and institutional affiliations.



Open Access This article is licensed under a Creative Commons Attribution 4.0 International License, which permits use, sharing, adaptation, distribution and reproduction in any medium or format, as long as you give appropriate credit to the original author(s) and the source, provide a link to the Creative Commons license, and indicate if changes were made. The images or other third party material in this article are included in the article's Creative Commons license, unless indicated otherwise in a credit line to the material. If material is not included in the article's Creative Commons license and your intended use is not permitted by statutory regulation or exceeds the permitted use, you will need to obtain permission directly from the copyright holder. To view a copy of this license, visit <http://creativecommons.org/licenses/by/4.0/>.

© The Author(s) 2024